1

The ABX_3 Perovskite Structure

1.1 Perovskites

Perovskite is a mineral of formula $CaTiO_3$. It was discovered in 1839 by the Prussian mineralogist Gustav Rose in mineral deposits in the Ural Mountains and named after the Russian mineralogist Count Lev Aleksevich von Petrovski. Natural crystals have a hardness of 5.5–6 and a density of 4000–4300 kg m^{-3}. They are usually dark brown to black, due to impurities, but when pure are clear with a refractive index of approximately 2.38. The crystal structure of this compound, initially thought to be cubic, was later shown to be orthorhombic (Table 1.1).

As with many minerals, Perovskite has given its name to a family of compounds called *perovskites*, which have a general formula close to or derived from the composition ABX_3. At present many hundreds of compounds are known that adopt the perovskite structure. In fact a perovskite structure mineral, Bridgmanite $(Fe,Mg)SiO_3$, is the most abundant solid phase in the Earth's interior, making up 38% of the total. The phase occurs between depths of approximately 660–2900 km but is only stable at high temperatures and pressures so that it is not found at the surface of the Earth.

To some extent the multiplicity of phases that belong to the perovskite family can be rationalised by assuming that perovskites are simple ionic compounds, where A is usually a large cation, B is usually a medium-sized cation and X is an anion.

Perovskites: Structure–Property Relationships, First Edition. Richard J. D. Tilley.

Table 1.1 *Representative ABX_3 perovskite phases*[a]

Phase	Space group[b]	Unit cell		
		a (nm)	*b* (nm)	*c* (nm)
1, 2				
$AgMgF_3$	C, $Pm\bar{3}m$ (221)	0.41162		
$CsPbI_3$	C, $Pm\bar{3}m$ (221)	0.62894		
$KCuF_3$	T, *I*4/*mcm* (140)	0.56086		0.76281
$KMgF_3$	C, $Pm\bar{3}m$ (221)	0.39897		
$KZnF_3$	C, $Pm\bar{3}m$	0.40560		
$NaMgF_3$	O, *Pbnm* (62)	0.48904	0.52022	0.71403
$NaFeF_3$	O, *Pnma* (62)	0.56612	0.78801	0.54836
NH_4ZnF_3	C, $Pm\bar{3}m$ (221)	0.41162		
1, 5				
$KTaO_3$	C, $Pm\bar{3}m$ (221)	0.40316		
$KNbO_3$	O, *Amm*2 (38)	0.3971	0.5697	0.5723
2, 4				
$SrTiO_3$	C, $Pm\bar{3}m$ (221)	0.3905		
$BaTiO_3$	T, *P*4*mm* (99)	0.39906		0.40278
$CaTiO_3$	O, *Pbmn* (62)	0.54035	0.54878	0.76626
$BaSnO_3$	C, $Pm\bar{3}m$ (221)	0.4117		
$CdSnO_3$	O, *Pnma* (62)	0.52856	0.74501	0.51927
$CaIrO_3$	O, *Pbnm* (62)	0.52505	0.55929	0.76769
$PbTiO_3$	T, *P*4*mm* (99)	0.3902		0.4143
$PbZrO_3$	O, *Pbam* (55)	0.58822	1.17813	0.82293
$SrCoO_3$	C, $Pm\bar{3}m$ (221)	0.3855		
$SrMoO_3$	C, $Pm\bar{3}m$ (221)	0.39761		
$SrRuO_3$	O, *Pnma* (62)	0.55328	0.78471	0.55693
$(Fe,Mg)SiO_3$	O, *Pnma* (62)	0.5020	0.6900	0.4810
3, 3				
$BiFeO_3$	Tr, *R*3*c* (161)	0.55798		1.3867
$BiInO_3$	O, *Pnma* (62)	0.59546	0.83864	0.50619
$ErCoO_3$	O, *Pbnm* (62)	0.51212	0.54191	0.73519
$GdFeO_3$	O, *Pbnm* (62)	0.53490	0.56089	0.76687
$HoCrO_3$	O, *Pnma* (62)	0.5518	0.7539	0.5245
$LaAlO_3$	Tr, *R*3*c* (161)	0.53644		1.31195
$LaCoO_3$	Tr, $R\bar{3}c$ (167)	0.54437		1.30957
$LaMnO_3$	O, *Pbnm* (62)	0.55367	0.57473	0.76929
$LaTiO_3$	O, *Pbnm* (62)	0.5576	0.5542	0.7587
$NdAlO_3$	Tr, $R\bar{3}c$ (167)	0.53796		1.31386
$PrRuO_3$	O, *Pnma* (62)	0.58344	0.77477	0.53794
$YbMnO_3$	O, *Pbnm* (62)	0.52208	0.58033	0.73053
4, 5				
$ThTaN_3$	C, $Pm\bar{3}m$	0.4020		

[a] Many of these phases are polymorphic, and lattice parameters vary with temperature and pressure.
[b] The crystal system, here and throughout the other tables in this book, is abbreviated thus: C, cubic; H, hexagonal; M, monoclinic; O, orthorhombic; T, tetragonal; Tr, trigonal (often specified in terms of a hexagonal unit cell); Tri, triclinic.

Naturally the overall ionic structure must be electrically neutral. If the charges on the ions are written as q_A, q_B and q_X, then

$$q_A + q_B = -3q_X$$

Frequently encountered (but not exclusive) combinations are

$$\begin{aligned}
q_X = -1, \quad & (q_A, q_B) = (1, 2); \text{ for example, } KNiF_3; \\
q_X = -2, \quad & (q_A, q_B) = (1, 5); \text{ for example, } NaNbO_3; \\
& (q_A, q_B) = (2, 4); \text{ for example, } CaTiO_3; \\
& (q_A, q_B) = (3, 3); \text{ for example, } LaAlO_3; \\
q_X = -3, \quad & (q_A, q_B) = (4, 5); \text{ for example, } ThTaN_3.
\end{aligned}$$

The importance of perovskites became apparent with the discovery of the valuable dielectric and ferroelectric properties of barium titanate, $BaTiO_3$, in the 1940s. This material was rapidly employed in electronics in the form of capacitors and transducers. In the decades that followed, attempts to improve the material properties of $BaTiO_3$ lead to intensive research on the structure – property relations of a large number of nominally ionic ceramic perovskite-related phases with overall compositions ABO_3, with a result that vast numbers of new phases were synthesised.

It was soon realised that, as a group, these materials possessed very useful physical and chemical properties far broader than those shown by $BaTiO_3$, and research widened to include a range of structures and phases that could all be related structurally to the perovskite family, including nominally ionic nitrides and oxynitrides. In addition, a number of materials which are better described as alloys, of formula A_3BX, where A and B are metals and X is an anion or semimetal, typically C, N, O and B are known. These are often said to adopt the so-called *antiperovskite* or *inverse perovskite* structure, because the metal A atoms occupy the positions corresponding to the anions in the ionic perovskites and the B and X atoms occupy sites corresponding to those occupied by the cations. The flexibility of the perovskite framework also allows it to include cations such as NH_4^+, which can often be considered to be spherical at normal temperatures. More complex phases, such as the inorganic–organic hybrid compounds $(CH_3NH_3)PbX_3$, where X is typically Cl, Br, I or a combination of these anions, have also been synthesised.

As well as phases with an ABX_3 composition, large numbers of modular structures have been prepared, all of which are built up, at least in part, from fragments, usually slabs, of perovskite-like structure. The formulae of these are not easily reconciled with a composition of ABX_3 until the structural building principles have been found and the nature of the interfaces between the various slabs is clarified.

For example, $Bi_2Ca_2Sr_2Cu_3O_{10+\delta}$, a superconducting oxide, is built from slabs of perovskite type separated by slabs of composition Bi_2O_2.

As would be expected, there is a close correlation between chemical and physical properties in these complex materials. It is this flexibility that makes the perovskites as a group, important, as the facile replacement of any of the atoms in this range of structures can be used to modify important physical properties in a controlled way. The flexibility comes at a structural cost. The ABX_3 perovskite structure is beset by structural variations that depend upon exact composition as well as temperature and pressure, all of which have a profound significance for physical properties. Moreover, many multi-cation or anion materials show an intricate microdomain structure when examined by transmission electron microscopy. These microdomains are small volumes of differing structural complexity that exist within a coherent anion matrix. Often they show ordering of atoms over several unit cell volumes with the pattern of order changing from one microdomain to its neighbours. When these microdomains are arranged throughout the crystal in a more or less random fashion, dependent upon the symmetry of the phase, the microscopic ordering is hidden from normal X-ray and neutron diffraction structure solving methods and may not feature in the refined structure of the macroscopic crystal studied. This level of order is generally revealed by high-resolution transmission electron microscopy. Because of this divergence, exact structural details of many perovskite phases of complex composition are open to question, although the overall broad-brush structure is known.

Fortunately much of this diversity can be understood or rationalised in terms of an ideal cubic perovskite structure. In this chapter the ideal ABX_3 perovskite structure is described together with some of the structural variations that occur which have significance for chemical and physical properties and which make precise structure determination a difficult task.

1.2 The Cubic Perovskite Structure: $SrTiO_3$

The idealised or *aristotype* perovskite structure is cubic and is adopted by $SrTiO_3$ at room temperature (but not at all temperatures). There are two general ways of listing the atoms in the cubic unit cell. The standard crystallographic description places the choice of origin at the Sr atom:

$SrTiO_3$: cubic; $a = 0.3905$ nm, $Z = 1$; space group, $Pm\bar{3}m$ (No. 221);

Atom positions: Sr: 1 (*a*) 0,0,0;
Ti: 1 (*b*) ½,½,½;
O: 3 (*c*) ½,½,0; ½,0,½; 0,½,½;

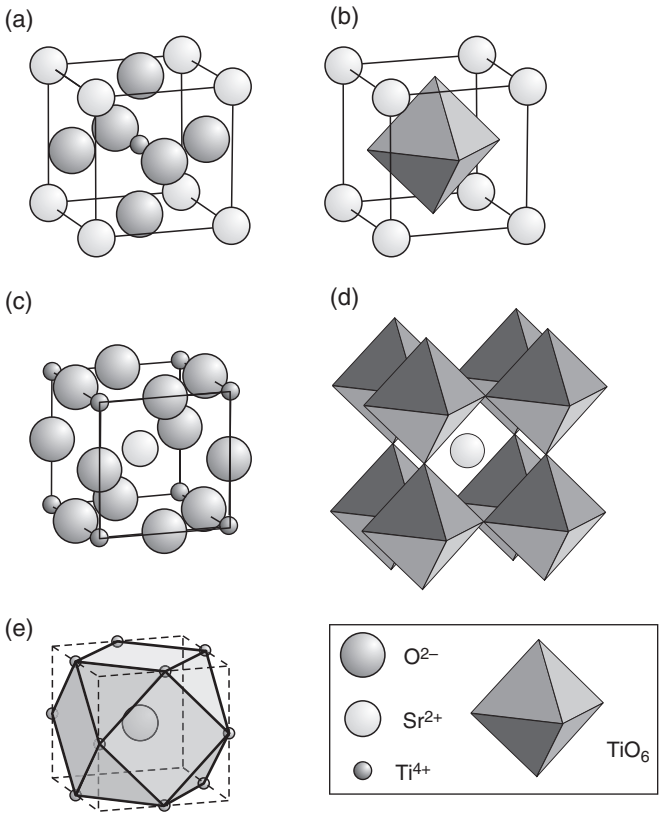

Figure 1.1 *The idealised perovskite structure of $SrTiO_3$: (a) atom positions with Sr^{2+} at cell origin; (b) TiO_6 octahedral coordination polyhedron; (c) atom positions with Ti^{4+} at cell origin; (d) TiO_6 octahedral polyhedron framework with Sr^{2+} at the cell centre; (e) cuboctahedral cage site*

The Sr^{2+} ions lie at the corners of the unit cell. The Ti^{4+} ions lie at the cell centre and are surrounded by a regular octahedron of O^{2-} ions (Figure 1.1a and b). For some purposes it is useful to translate the cell origin to the Ti^{4+} ions:

$$\begin{aligned}\text{Atom positions}: \ &\text{Ti}: 1(a)\, 0,0,0;\\ &\text{Sr}: 1(b)\, ½,½,½;\\ &\text{O}: 3(d)\, ½,0,0;\ 0,½,0;\ 0,0,½;\end{aligned}$$

The large Sr^{2+} ions are coordinated to 12 O^{2-} ions and are now situated at the unit cell centre (Figure 1.1c). For a discussion of the chemical and physical properties of this (and other) perovskites, it is convenient to think of the structure as built-up from an array of corner sharing TiO_6 octahedra (Figure 1.1d). The large Sr^{2+} ions are located at

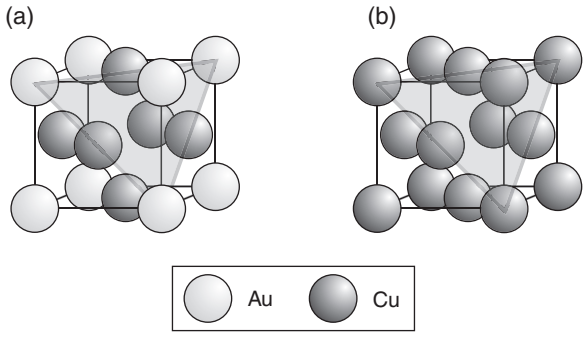

Figure 1.2 *(a) The $AuCu_3$ and (b) the Cu (A1, fcc) structure*

the unit cell centre and are surrounded by a cuboctahedral cage of O^{2-} ions (Figure 1.1e). The TiO_6 framework is regular and the octahedra are parallel to each other. All the Ti^{4+}—O^{2-} bond lengths are equal and the six O^{2-}—Ti^{4+}—O^{2-} bonds are linear.

The Sr^{2+} and O^{2-} positions in the $SrTiO_3$ structure are identical to that of the Au and Cu positions in the alloy Cu_3Au, and if the difference between the Sr^{2+} and O^{2-} ions (or Cu and Au atoms) is ignored, they form a cubic array identical to that of the Cu structure (Figure 1.2a and b). This latter is the simple A1 structure type, often described as the face-centred cubic (fcc) structure, which is made up of (111) planes that lie normal to the cell body diagonal [111], stacked in the normal face-centred sequence … ABCABC…. Thus the $SrTiO_3$ structure can also be thought of as a built-up from close-packed layers of (111) planes containing ordered Sr^{2+} and O^{2-} ions that lie normal to the cubic unit cell body diagonal [111]. The charge balance needed to maintain charge neutrality in this skeleton structure is provided by an ordered distribution of the Ti^{4+} ions in the available octahedral interstices that are bounded by O^{2-} ions only (Figure 1.3).

It is often convenient when describing the structures of more complex perovskite-related phases (Chapters 2 and 3) to display the structure as linked ideal TiO_6 octahedra. The conventional view of the ideal perovskite structure (Figure 1.4a) is often shown tilted to make the (111) layers almost or exactly horizontal (Figure 1.4b and c). More often the alkaline earth atoms are omitted and just the octahedral framework is shown (Figure 1.4d and e). Other projections, such as down [111], show the octahedra projected as hexagonal outlines or down [110] as diamond outlines (Figure 1.4f and g).

1.3 The Goldschmidt Tolerance Factor

From a crystallographic perspective, the ideal perovskite structure is inflexible, as the unit cell has no adjustable atomic position parameters, so that any compositional change must be accommodated by a change in lattice parameter. This is a

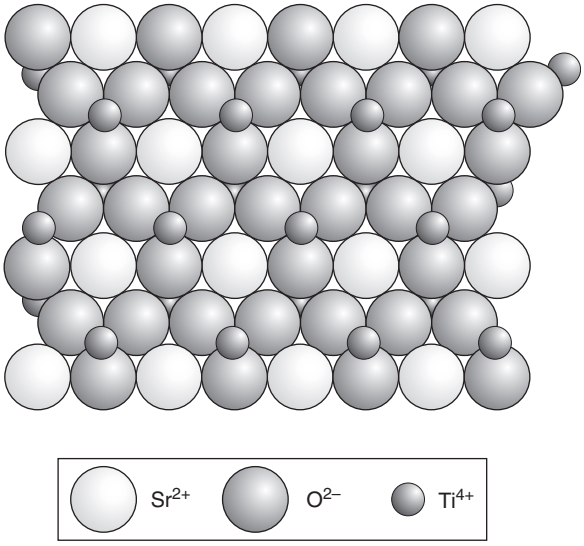

Figure 1.3 *A single SrO_3 (111) plane in $SrTiO_3$. The Ti^{4+} ions, above and below the SrO_3 layer, occupy octahedral interstices that are bounded by six O^{2-} ions*

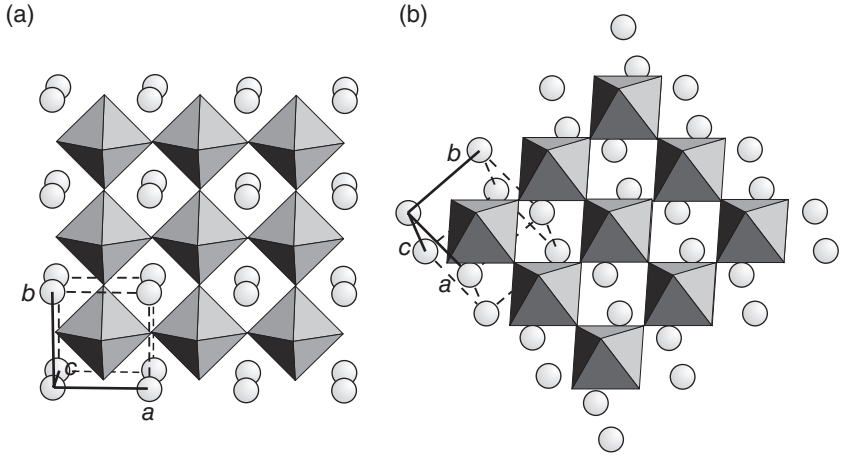

Figure 1.4 *The cubic $SrTiO_3$ perovskite structure (a) conventional view with $3 \times 3 \times 1$ unit cells displayed; (b) the same rotated by approximately 45°; (c) the same rotated further so that one set of SrO_3 planes lies normal to the plane of the page; (d and e) as (b and c) showing only the TiO_6 octahedral framework; (f) octahedral framework projected down [111]; (g) octahedral framework projected down [110]*

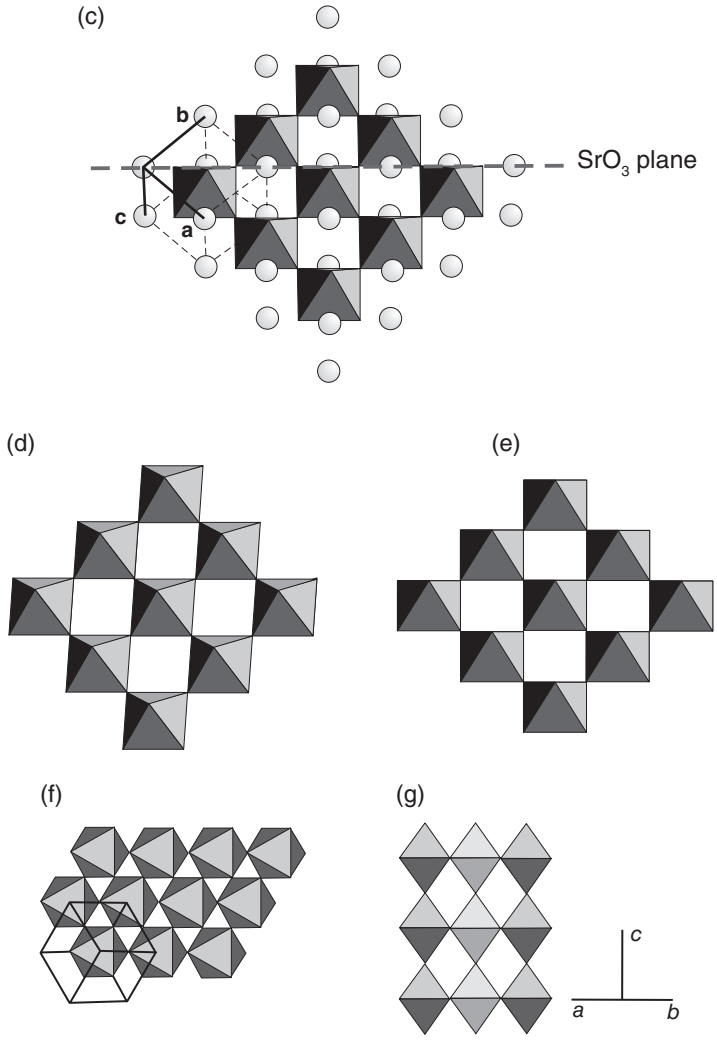

Figure 1.4 *(Continued)*

simple sum of anion – cation bond lengths. The cubic unit cell edge, a, is equal to twice the B—X bond length:

$$2(\mathrm{B}-\mathrm{X}) = a$$

The width of the cuboctahedral cage site, $\sqrt{2}a$, is equal to twice the A—X bond length:

$$2(\mathrm{A}-\mathrm{X}) = \sqrt{2}a$$

This means that the ideal structure forms when the ratio of the bond lengths is given by:

$$\frac{(\text{A—X})}{(\text{B—X})} = \sqrt{2}$$

or

$$\frac{(\text{A—X})}{\sqrt{2}(\text{B—X})} = 1$$

This relationship was first exploited by Goldschmidt, in 1926, who suggested that it could be used to predict the likelihood that a pair of ions would form a perovskite structure phase. When this was initially proposed, very few crystal structures had been determined and so ionic radii were used as a substitute for measured bond lengths. For this purpose, it is assumed that for a stable structure to form the cations, just touch the surrounding anions (Goldschmidt's rule), then:

$$\frac{(r_A + r_X)}{(r_B + r_X)} = \sqrt{2}$$

or

$$t = \frac{(r_A + r_X)}{\sqrt{2}(r_B + r_X)} = 1\,(\text{ideal structure})$$

where t is called the *tolerance factor*, r_A is the radius of the cage site cation, r_B is the radius of the octahedrally coordinated cation and r_X is the radius of the anion. Goldschmidt's proposal was that a perovskite structure phase would form if the value of the tolerance factor, t, was close to 1.0.

Note that it is necessary to use ionic radii appropriate to the coordination geometry of the ions. Thus r_A should be appropriate to 12 coordination, r_B to octahedral coordination and r_X to linear coordination. Furthermore, it is best to use radii scales that mirror the X anion present, as radii appropriate to oxides, although a reasonable approximation for fluorides, are poor when applied to chlorides and sulphides.

Because many perovskite structures have been described, it is now usual to use the measured bond lengths in the crystal rather than ionic radii to give an *observed tolerance factor* t_{obs}:

$$t_{obs} = \frac{(\text{A—X})}{\sqrt{2}(\text{B—X})}$$

where (A—X) is the average of the measured bond lengths between the A cation and the surrounding 12 anions and (B—X) is the average of the measured bond lengths between the B cation and the surrounding six anions. It is found that for specific groups of perovskites (e.g. $ATiO_3$ titanates, $AAlO_3$ aluminates), there is a linear relationship between t_{obs} and t which varies slightly from one family to another.

Despite its simplicity, the tolerance factor has reasonable predictive power, especially for oxides, where ionic radii are known with greatest precision. Ideally t should be equal to 1.0 and it has been found empirically that if t lies in the approximate range 0.9–1.0 a cubic perovskite structure is a reasonable possibility. If $t > 1$, that is, large A and small B, a hexagonal packing of the AX_3 layers is preferred and hexagonal phases of the $BaNiO_3$ type form (Chapter 3). In cases where t of the order of 0.71–0.9, the structure, particularly the octahedral framework, distorts to close down the cuboctahedral coordination polyhedron, which results in a crystal structure of lower symmetry than cubic. For even lower values of t, the A and B cations are of similar size and are associated with the ilmenite, $FeTiO_3$, structure or the C-type rare earth Ln_2O_3 structure.

In the case of chlorides and sulphides, the tolerance factor tends to move downwards compared to that for oxides and fluorides so that cubic and distorted cubic phases form for t in the range 0.8–0.9, and hexagonal perovskites form if t is greater than 0.9.

The concept of the tolerance factor can be extended to perovskites with more complex compositions by using an average value for ionic radii or bond length. For example, for an A-site substituted phase $A_{1-x}A'_xBX_3$, one can write

$$t = \frac{\left[(1-x)r_A + xr_{A'} + r_X\right]}{\sqrt{2}\left(r_B + r_X\right)}$$

and in the case of B-site substitution $AB_{1-x}B'_xX_3$:

$$t = \frac{\left(r_A + r_X\right)}{\sqrt{2}\left[(1-x)r_B + xr_{B'} + r_X\right]}$$

Similarly, in terms of bond lengths:

$$t_{obs} = \frac{<A–X>}{\sqrt{2}\ <B–X>}$$

where <A–X> signifies the average bond length for the links A–X, A′–X, etc. and <B–X> signifies the average bond length for the links B–X, B′–X, etc. Both equations can be generalised to more complex structures (A, A′, A″…) (B, B′, B″…) $(X, X', X''\ldots)_3$.

1.4 ABX_3 Perovskite Structure Variants

The BX_6 octahedra are the root of many of the important physical properties of perovskites, such as magnetic and ferroelectric responses to external fields. This is because these are often mediated by the electron configurations of the B cations, which themselves are modified by the surrounding geometry of the six anions. The A cations, although they cannot be ignored, tend to be closed-shell ions with a fixed valence and so less responsive to chemical manipulation with a view to modification of chemical and physical properties. Thus it is useful to place the distortions that occur in perovskites due to the shape and relative orientation of the BX_6 polyhedra into a crystallographic framework.

The simplest change that can be envisaged is that in which the BX_6 octahedra remain perfect (or nearly so) and the cations are simply displaced away from the centre of the octahedron. Cation displacement is usually associated with cations that are 'too small' for the octahedral site, leading to a tolerance factor significantly less than 1 (although in fact B-cation size is only one of several factors of importance in this distortion). The structure now becomes tetragonal, trigonal or orthorhombic, depending upon the direction of cation displacement and the magnitude of the displacements which occur. In addition, the displacements produce permanent electric dipoles in the unit cell and can give rise to pyroelectric, ferroelectric and antiferroelectric effects (Chapter 6).

A second structural response which preserves the perfect (or nearly perfect) BX_6 octahedral geometry is octahedral tilt or rotation. This response is mostly associated with A cations that are too small for the cuboctahedral cage site, and so the BX_6 octahedra twist so as to effectively reduce the cavity dimensions, again allowing the structure to accommodate values of t less than 1. As with cation displacement, rotation also lowers the symmetry of the crystal (Section 1.7) and has a profound influence on the physical properties of these phases.

Finally, the BX_6 octahedron itself can distort to give elongated or flattened octahedra, which in extreme cases can lead to square planar or square pyramidal coordination. These distortions are a result of interactions between the cation electron orbitals and the surrounding anions, typified by the Jahn–Teller effect (Section 1.6). Octahedral distortion can also be caused by cation valence changes such as disproportionation:

$$2B^{n+} \rightarrow B^{n+1} + B^{n-1}$$

The two different-sized cations then may adjust to the surroundings by a distortion of one or both of the cation-centred BX_6 octahedra to give rise to two different-sized octahedra.

These three modifications, namely, B-cation displacement, BX_6 tilt/rotation and BX_6 distortion, are not mutually exclusive and they can occur independently or, often, in combination with one another. Moreover, the resulting changes may be cooperative in that they affect all octahedra in a similar way, or non-cooperative, in which case the distortions may cancel out at a macroscopic level although they may still influence microscopic properties.

The amounts of distortion are generally small and are readily influenced by the ambient conditions. Thus changes in temperature, pressure, crystallite size or form may alter the degree of distortion or the type of distortion present. The majority of perovskite phases manifest a series of symmetry changes as the temperature or pressure is changed, usually resulting in a cubic form at higher temperatures and pressures. For example, the perovskite $SrSnO_3$, which is orthorhombic, space group *Pmna*, at room temperature, changes as the temperature increases to orthorhombic, space group *Imma*, at 905 K, to tetragonal, space group *I*4/*mcm* at 1062 K and finally to cubic space group $Pm\bar{3}m$ at 1295 K.

For many of these lower symmetry forms, the shift from the ideal cell is small or can be neglected for some purposes, and in such cases it is often convenient to refer these structures to an idealised pseudocubic structure, of cell length a_p (equivalent to a for ideal $SrTiO_3$, 0.39 nm), that can be used as a first (and often sufficient) approximation in describing the properties of the phases.

1.5 Cation Displacement: $BaTiO_3$ as an Example

Cation displacement in $BaTiO_3$ is attributed to the second order (or pseudo) Jahn–Teller effect, acting upon the d^0 Ti^{4+} ion. This mechanism applies to nonlinear molecules with a nondegenerate electronic ground state accompanied by a very low-lying excited state. Under these conditions, distortions of symmetry occur that facilitate the mixing of the electronic ground and excited states in a way to lower the ground-state energy. In perovskites, the appropriate symmetry change is provided by cation displacement. (The first-order Jahn–Teller effect, which affects d^n cations, is described in Section 1.6.)

To preserve a maximum degree of symmetry, cation displacement needs to be along one of the symmetry axes of the octahedron. There are three tetrad (fourfold) axes of rotational symmetry, each passing through opposite vertices of the octahedron; four triad (threefold) axes of rotational symmetry, each passing through the centres of opposing triangular faces of the octahedron and six diad (twofold) axes

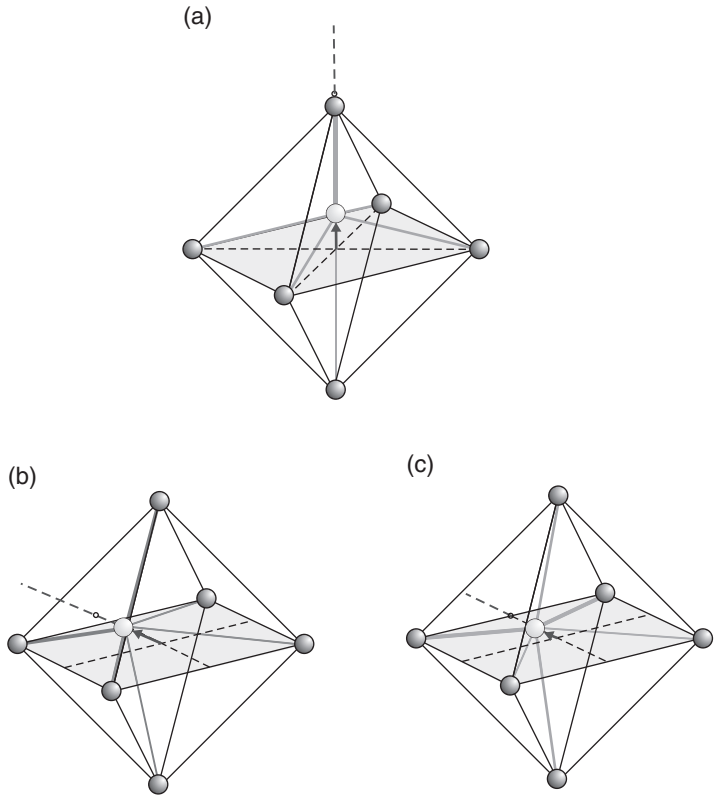

Figure 1.5 *Cation displacement in a BX_6 octahedron: cation displacement along (a) a tetrad axis; (b) a triad axis; (c) a diad axis*

of rotational symmetry, each passing though the centres of opposite edges of the octahedron (see Figure 1.10). The symmetry axis parallel to the direction of the displacement is maintained after the displacement. Cation displacement parallel to one of the tetrad axes ideally gives rise to one longer bond, one shorter bond and four bonds of intermediate length (Figure 1.5a). Cation displacement along a triad axis ideally gives rise to three shorter bonds and three longer bonds (Figure 1.5b), while cation displacement along a diad ideally gives rise to two long and two short bonds in the plane containing the diad and two bonds of intermediate length roughly perpendicular to that plane (Figure 1.5c). The simplest structures are found when all of the cation displacements are identical and in such cases, B-cation displacement is usually accompanied by smaller A-cation displacement.

The effects of B-cation displacement upon the structures and dielectric properties of perovskite phases have been extensively studied in the important dielectric/ferroelectric perovskite, $BaTiO_3$. The phase shows transformations from trigonal to

orthorhombic (at 183 K), orthorhombic to tetragonal (at 263 K) and tetragonal to cubic (at 393 K), all due to cation displacement.

The high-temperature phase, stable above 393 K, adopts the ideal perovskite structure: space group $Pm\bar{3}m$ (221), $a = 0.39732$ nm (Figure 1.6a). The medium-sized Ti^{4+} ions are situated at the centre of an octahedron of oxygen ions with equal bond lengths of approximately 0.2 nm, while the large Ba^{2+} cations are in the centres of the cuboctahedral cage sites, surrounded by 12 oxygen ions.

Between 393 and 268 K the unit cell is tetragonal and ferroelectric. As the crystal cools through the cubic – tetragonal transition temperature, the cubic cell expands slightly along one edge to produce the tetragonal **c**-axis and is slightly compressed along the other two edges to form the tetragonal **a**- and **b**-axes: space group *P*4*mm* (99). $a = b = 0.39910$ nm, $c = 0.40352$ nm (Figure 1.6b). The change from cubic to tetragonal is accompanied by an off-centre movement of the octahedrally coordinated Ti^{4+} ions along the **+c**-axis, which is one of the tetrad axes of the octahedron (Figure 1.6c). The O^{2-}—Ti^{4+} bond lengths parallel to the **c**-axis are now ≈0.22 and ≈0.18 nm, while the equatorial bond lengths remain at ≈0.2 nm. The change in the Ba^{2+} positions is almost negligible. The Ti^{4+} displacement is accompanied by a slight change in octahedron dimensions so that two equatorial oxygen atoms move parallel to the **+c**-axis and two move in the opposite direction. These displacements give rise to electric dipoles, *p*, one in each octahedron (Figure 1.6d) that are the source of the ferroelectric properties of tetragonal $BaTiO_3$. There is no preference as to which of the original cubic axes becomes the polar direction, and so this can take one of six equivalent directions, so that a single crystal invariably becomes heavily twinned on cooling.

Between the temperatures 263 and 183 K, the tetragonal structure undergoes a further transition with the Ti^{4+} cation displaced along a diad axis (Figure 1.6e) giving four Ti—O bonds approximately 0.198 nm and two bonds approximately 0.201 nm in length, with once again a slight distortion of the octahedra, producing an ordered array of electronic dipoles. This results in an elongation along a face diagonal of the pseudocubic unit cell to give an orthorhombic phase: space group *Amm*2 (38), $a = 0.39594$ nm, $b = 0.56266$ nm, $c = 0.56435$ nm (Figure 1.6f).

Below 183 K the Ti^{4+} cation displacement is along the triad axis, giving rise to three shorter Ti—O bonds of approximately 0.21 nm and three bonds of ≈0.19 nm in length (Figure 1.6g). The pseudocubic cell is now elongated along the cell body diagonal to produce a rhombohedral cell: space group *R*3*m* (160), $a = 0.40043$ nm, $\alpha \approx 89.86°$ (Figure 1.6h). This cell is very close in dimensions to the cubic high-temperature structure but again displays a ferroelectric response to applied electric fields, which the cubic phase does not.

All of the phases described and the cations displacements and octahedral distortions are temperature and pressure sensitive. The phase diagram for $BaTiO_3$ at

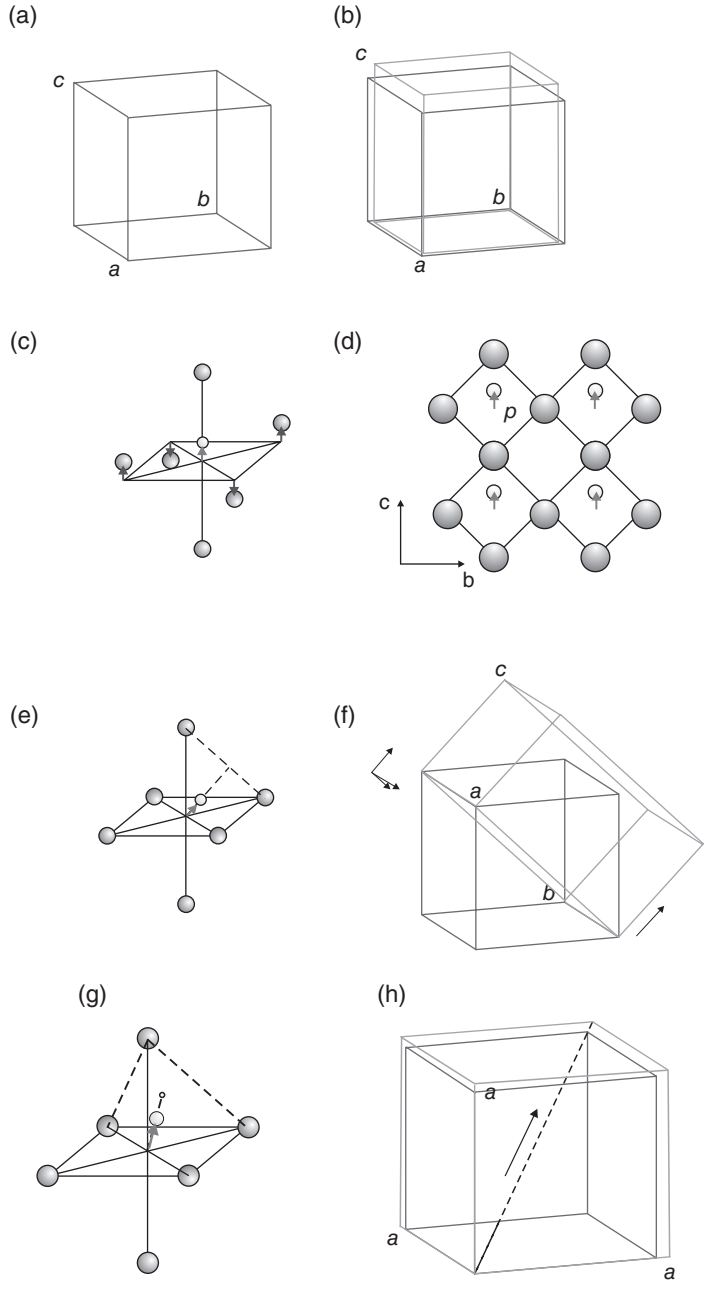

Figure 1.6 *Cation displacements (exaggerated for clarity) in $BaTiO_3$: (a) T > 398 K, cubic; (b) 398 > T > 278 K, tetragonal; (c) ion displacements in each TiO_6 octahedron; (d) electric dipoles generated by Ti^{4+} ion displacements; (e) Ti^{4+} ion displacement in the orthorhombic phase; (f) orthorhombic unit cell compared cubic unit cell; (g) Ti^{4+} ion displacement in the trigonal phase; (h) rhombohedral unit cell compared to cubic unit cell*

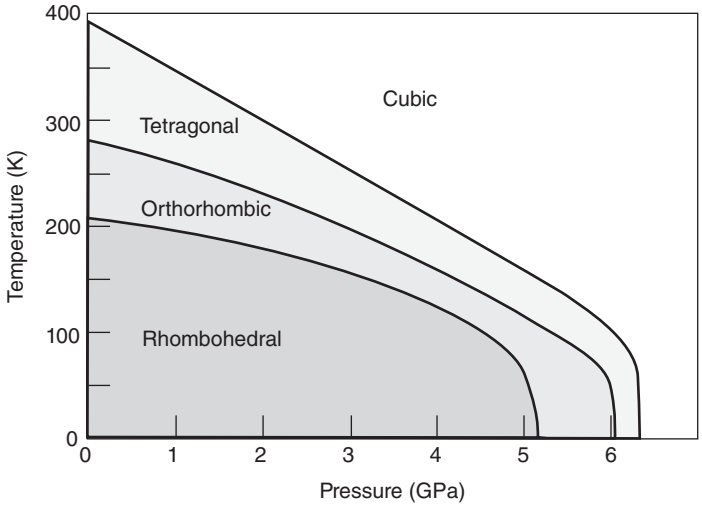

Figure 1.7 *The temperature–pressure phase diagram of* $BaTiO_3$ *(Original data in Hayward and Salje (2002) and Ishidate* et al. *(1997))*

moderate temperatures and pressures illustrates the symmetry changes encountered (Figure 1.7). It is seen that, at 300 K and ambient pressure (1 atm = 0.000101 GPa), $BaTiO_3$ will exist as the tetragonal form. When the applied pressure reaches approximately 2 GPa, both the cubic and tetragonal forms will coexist. A slight increase in either pressure or temperature will tip the balance in favour of the cubic form, which will then exist alone.

Note that these changes are also influenced by particle size and morphology. Nanoparticles often present a different pattern of crystallographic behaviour than that illustrated.

1.6 Jahn–Teller Octahedral Distortion: $KCuF_3$ as an Example

The best known examples of octahedral distortion in perovskites are Jahn–Teller distortions. These arise from the (first order) Jahn–Teller effect, which, in the broadest sense, applies to all nonlinear molecules. The Jahn–Teller theorem says that a molecule with a symmetrical atomic configuration and a degenerate electronic ground state is unstable and will distort so as to remove the electronic degeneracy. With respect to perovskite structures, the Jahn–Teller theorem applies to octahedrally coordinated transition metal B-site cations. It implies that perovskites containing ions with certain d-electron configurations (so-called Jahn–Teller ions) will have an enhanced stability when located in

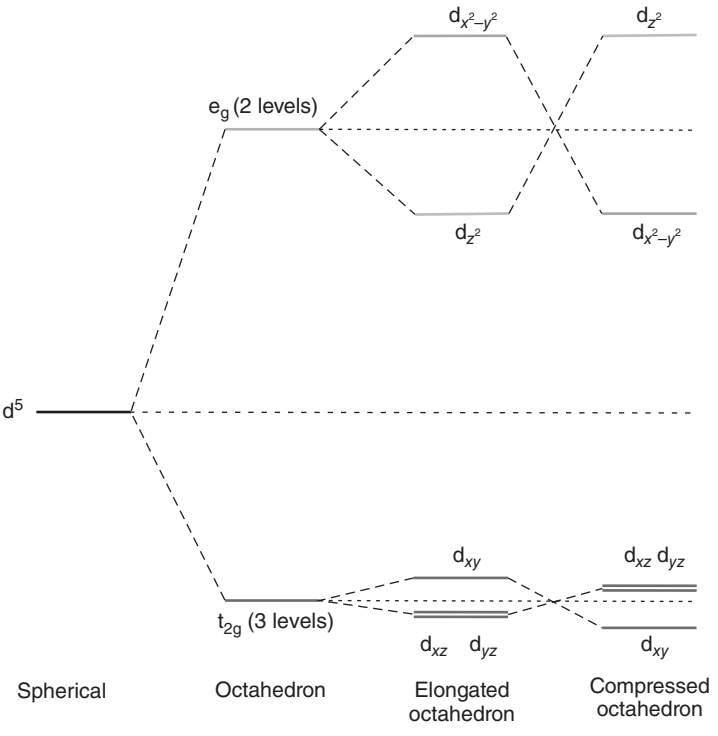

Figure 1.8 *The effect of a Jahn–Teller distortion on the d-electron energy levels of a B-site cation in an octahedron*

a distorted octahedral environment compared to that in an undistorted one. The distortion may take the form of an elongation of each octahedron along one of its fourfold tetrad symmetry axes, giving a coordination polyhedron with four shorter B—X bonds and two longer B—X bonds or the converse, with four longer B—X bonds and two shorter B—X bonds, leading to a compressed octahedron.

The degenerate ground state comes about in the following way. In an ideal octahedron the d-electron energy levels split into two groups, a lower energy triply degenerate pair, labelled t_{2g}, consisting of the d_{xy}, d_{yz} and d_{xz} orbitals, and an upper doubly degenerate pair labelled e_g, consisting of the orbital pair $d_{x^2-y^2}$ and d_{z^2} (Figure 1.8). A transition metal ion with an odd number of electrons in the upper (e_g) pair of d orbitals, such as high-spin Cr^{2+}, Mn^{3+} (d^4, $t_{2g}^3e_g^1$); low-spin Co^{2+}, Ni^{3+} (d^7, $t_{2g}^6e_g^1$) and Cu^{2+} (d^9, $t_{2g}^6e_g^3$) will have a degenerate ground state because there are a two equivalent electron distributions possible. For example, with Mn^{3+} one electron can be placed in either the $d_{x^2-y^2}$ or d_{z^2} orbital to give the degenerate energy configurations $t_{2g}^3, d_{x^2-y^2}^1 d_{z^2}^0$ or $t_{2g}^3\ d_{z^2}^1 d_{x^2-y^2}^0$. The same degeneracy will occur for the

other ions listed. An elongation or compression of the octahedron will remove the degeneracy by a further splitting of the both the t_{2g} and e_g groups (Figure 1.8). The change in the t_{2g} group is rather small and is not of greatest importance for perovskites. The splitting of the e_g group is, however, significant and does lead to octahedral distortion. It is not possible to determine from these qualitative descriptions whether the favoured distortion will be octahedral elongation or compression, but by far the commonest in perovskites is an elongation of the octahedron, which in extreme cases can give rise to square pyramidal or square planar coordination.

In general the A and B ions remain in the centres of the coordination polyhedra in spite of the distortion, but the symmetry of the unit cell drops to tetragonal or orthorhombic. The distortion is both temperature and pressure sensitive, and perovskites showing Jahn–Teller distortion generally return to cubic symmetry at higher temperatures and pressures.

An example that has been investigated in detail is $KCuF_3$, containing the Jahn–Teller ion Cu^{2+}. Here the electronic energy level degeneracy in a perfect octahedron corresponds to the alternative electron distributions $d^2_{x^2-y^2}d^1_{z^2}$ or $d^1_{x^2-y^2}d^2_{z^2}$. The Jahn–Teller distortion is apparent in the elongated form of the CuF_6 octahedra.

$KCuF_3$: tetragonal; $a = b = 0.58550$ nm, $c = 0.78456$ nm, $Z = 4$; space group, *I*4/*mcm* (No. 140), at 295 K and normal pressure;

Atom positions: Kr: 4 (a) 0,0,¼; 0,0,¾;
Cu: 4 (d) 0,½,0; ½,0,0;
F1: 4 (b) 0,½,¼; ½,0,¼;
F2: 8 (h) $x, x+½, 0; -x, -x+½, 0; -x+½, x, 0; x+½, -x, 0$;
$x = 0.2281$

The CuF_6 octahedra have one axis elongated to give a Cu—F bond length of 0.225 nm, while the other two are shortened unequally to 0.196 and 0.189 nm (Figure 1.9a and b). The sheets of octahedra lie on planes at $z = 0$ and $z = ½$. All are positioned so that one of the short diameters lies parallel to [001], but within any one sheet of structure parallel to (001), the long dimensions are arranged so that they lie perpendicular to those of the neighbouring octahedra (Figure 1.9c). The perovskite pseudocubic cell has dimensions $a_p = a/\sqrt{2} = c/2 \approx 0.40$ nm.

The distortion varies with temperature and pressure in a uniform way. When the pressure increases to 8 GPa, the four shorter bonds become almost equal in length and the long bonds shorten considerably to give an approximately regular octahedral coordination polyhedron.

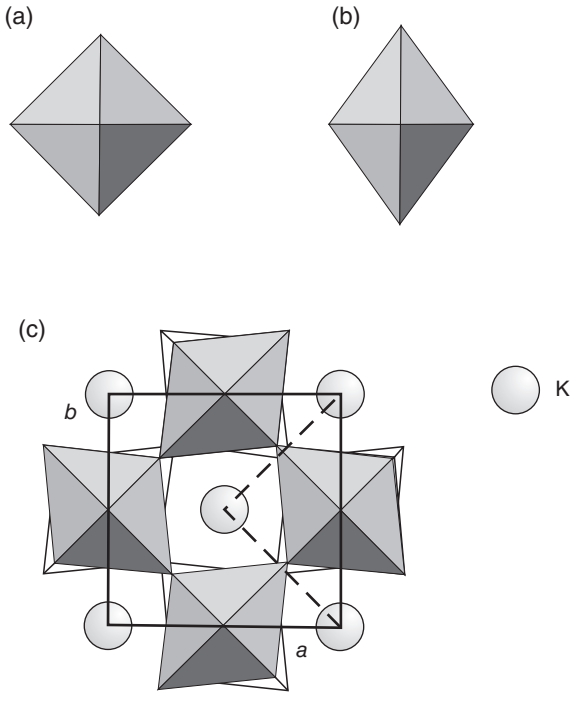

Figure 1.9 *The $KCuF_3$ structure: (a) a regular CuO_6 octahedron; (b) CuO_6 octahedron elongated along one tetrad axis; (c) the $KCuF_3$ structure projected down [001]. The distorted octahedra in the lower layer are shown in outline, and those in the upper layer are shown shaded. The unit cell is outlined and the pseudocubic cell is dotted*

1.7 Octahedral Tilting

1.7.1 Tilt Descriptions

The (ideally rigid) apex-linked BX_6 octahedra can be imagined to be joined by flexible hinges that allow for a certain amount of rotation or tilting. In many cases, slight tilting of the octahedra, so as to enhance stability, is associated with A cations that are slightly too small to fit the ideal structure, as in the example of perovskite, $CaTiO_3$, itself, which displays an orthorhombic symmetry compared to cubic $SrTiO_3$. The tilting contrives to reduce the size of the A-site cavity slightly and so is a mechanism of compensation for a mismatch in the A—X/B—X bond lengths. Tilting can occur about the (a) tetrad, (b) diad and (c) triad axes of the octahedron (Figure 1.10).

The corner connectivity of the BX_6 octahedra means that the tilt of one octahedron completely determines the tilting in the plane perpendicular to the tilt axis

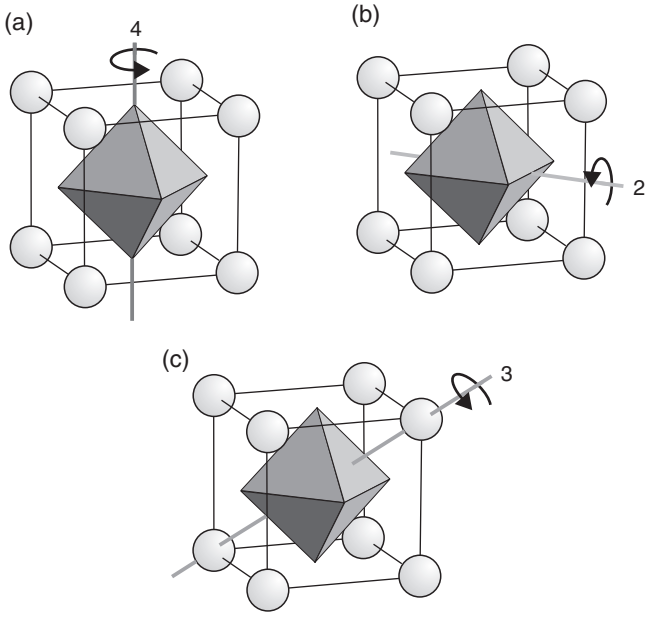

Figure 1.10 *Tilt axes of an octahedron: (a) one of three tetrad axes; (b) one of six diad axes; (c) one of four triad axes*

(Figure 1.11). In addition, the tilting in an adjacent plane must imitate that in the first, but can be in phase with it (i.e. exactly the same when viewed down the tilt axis) or out of phase with it (i.e. in the opposite direction).

The tilting of the octahedra can also be envisaged in terms of rotations compounded of three component tilts along the *x*-, *y*- and *z*-axes of the parent ideal perovskite structure. The system of nomenclature most frequently encountered is that of Glazer (1972). A rotation is described by a symbol *a*, *b* or *c* for tilt axes parallel to *x*, *y* and *z*. If there is no tilt, the superscript 0 is added, and if the tilt is exactly the same about two axes, then the letter symbol is repeated. In this way, the ideal perovskite structure is given the symbol $a^0a^0a^0$, signifying no tilt about *x*, *y* or *z* (Figure 1.12a). A rotation around *z* can give two layers of octahedra with exactly the same relative orientation, $a^0a^0c^+$ (Figure 1.12b), or with opposite relative orientations $a^0a^0c^-$ (Figure 1.12c). Similarly, three equal tilts, $a^-a^-a^-$, give a structure with each layer of octahedra with the same relative orientation (Figure 1.12d) while the opposite relative orientation of the two layers of octahedra is produced by $a^-a^-c^+$ (Figure 1.12e). Furthermore, three equal tilts correspond to a rotation $\varphi°$ about triad [111]-type axis while two equal tilts corresponds to rotation $\theta°$ about a diad [110]-type axis, provided that tilt angles are fairly small, say less than about 15°, and one tilt corresponds to a rotation $\varphi°$ about a tetrad [100]-type axis.

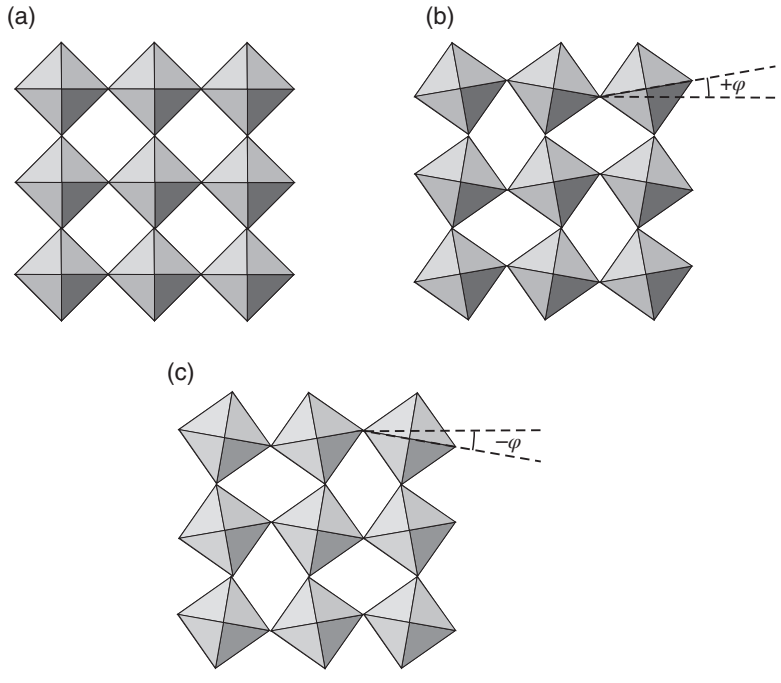

Figure 1.11 *Tilting of a plane of corner-linked octahedra about a tetrad axis perpendicular to the plane of the figure through one octahedron: (a) no tilt; (b) a tilt of +φ; (c) a tilt of −φ*

In the simplest case, and considering only a two-octahedron repeat along each of the cubic or pseudocubic axes, 10 possible tilt combinations are possible:

three tilts; $a^+b^+c^+$, $a^+b^+c^-$, $a^+b^-c^-$, $a^-b^-c^-$;
two tilts; $a^0b^+c^+$, $a^0b^+c^-$, $a^0b^-c^-$;
one tilt; $a^0a^0c^+$, $a^0a^0c^-$;
no tilts; $a^0a^0a^0$;

In order to relate these to crystallographic structures, it is necessary to take into account the relative magnitudes of the tilts. In this case, three unequal tilts produce three unequal pseudocubic axes, two equal tilts and one different tilt produce two equal pseudocubic axes and one different and three equal tilts produce three equal pseudocubic axes. Moreover, whenever a superscript is 0 or +, a mirror plane must exist perpendicular to the tilt axis. By examination of the 10 tilt combinations described in terms of these and related constraints, 23 different tilt systems can be derived together with the pseudocubic unit cell dimensions and the ideal space group of the four octahedra unit cell (Table 1.2). It is, though, important to

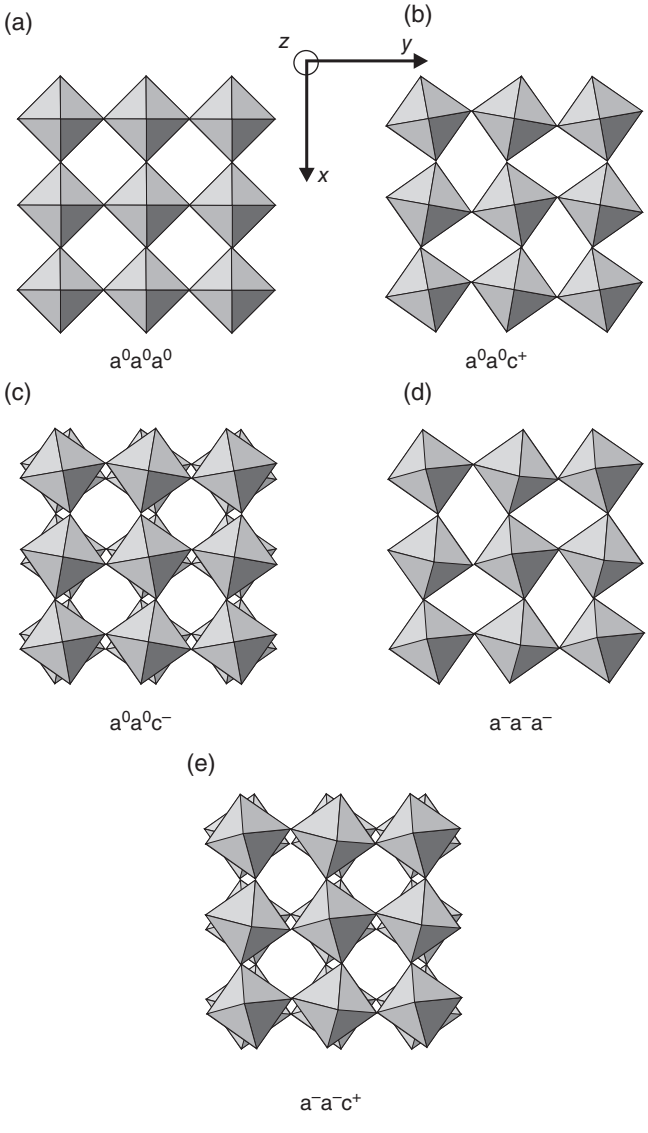

Figure 1.12 *Glazer tilt notation: (a) $a^0a^0a^0$; (b) $a^0a^0c^+$; (c) $a^0a^0c^-$; (d) $a^-a^-a^-$; (e) $a^-a^-c^+$*

remember should a perovskite phase have a repeat of more than two octahedra in each axial direction, a more complex notation will be needed.

The lattice parameters of many of the resulting unit cells can be related to the B—O bond distance, d, and the angles of rotation, φ about a tetrad axis [001], θ about a diad axis [110] and φ about a triad axis [111]. The simplest of these are given in Table 1.3.

Table 1.2 *Tilt systems for BX_6 octahedra in ABX_3 perovskites*

Number	Symbol	Pseudocubic unit cell	Space group
Three tilts			
1	$a^+b^+c^+$	$a_p \neq b_p \neq c_p$	*Immm* (71)
2	$a^+b^+b^+$	$a_p \neq b_p = c_p$	*Immm* (71)
3	$a^+a^+a^+$	$a_p = b_p = c_p$	$Im\bar{3}$ (204)
4	$a^+b^+c^-$	$a_p \neq b_p \neq c_p$	*Pmmn* (59)
5	$a^+a^+c^-$	$a_p = b_p \neq c_p$	$P4_2/nmc$ (137)
6	$a^+b^+b^-$	$a_p \neq b_p = c_p$	*Pmmn* (59)
7	$a^+a^+a^-$	$a_p = b_p = c_p$	*Pmmn* (59)
8	$a^+b^-c^-$	$a_p \neq b_p \neq c_p$ $\alpha \neq 90°$	$P2_1/m$ (11)
9	$a^+a^-c^-$	$a_p = b_p \neq c_p$ $\alpha \neq 90°$	$P2_1/m$ (11)
10	$a^+b^-b^-$	$a_p \neq b_p = c_p$ $\alpha \neq 90°$	*Pnma* (62)
11	$a^+a^-a^-$	$a_p = b_p = c_p$ $\alpha \neq 90°$	*Pnma* (62)
12	$a^-b^-c^-$	$a_p \neq b_p \neq c_p$ $\alpha \neq \beta \neq \gamma \neq 90°$	$P\bar{1}$ (2)
13	$a^-b^-b^-$	$a_p \neq b_p = c_p$ $\alpha \neq \beta \neq \gamma \neq 90°$	*C*2/*c* (15)
14	$a^-a^-a^-$	$a_p = b_p = c_p$ $\alpha = \beta = \gamma \neq 90°$	$R\bar{3}c$ (167)
Two tilts			
15	$a^0b^+c^+$	$a_p < b_p \neq c_p$	*Immm* (71)
16	$a^0b^+b^+$	$a_p < b_p = c_p$	*I*4/*mmm* (139)
17	$a^0b^+c^-$	$a_p < b_p \neq c_p$	*Cmcm* (63)
18	$a^0b^+b^-$	$a_p < b_p = c_p$	*Bmmb* (63)
19	$a^0b^-c^-$	$a_p < b_p \neq c_p$ $\alpha \neq 90°$	*C*2/*m* (12)
20	$a^0b^-b^-$	$a_p < b_p = c_p$ $\alpha \neq 90°$	*Imma* (74)
One tilt			
21	$a^0a^0c^+$	$a_p = b_p < c_p$	*P*4/*mbm* (127)
22	$a^0a^0c^-$	$a_p = b_p < c_p$	*I*4/*mcm* (140)
Zero tilt			
23	$a^0a^0a^0$	$a_p = b_p = c_p$	$Pm\bar{3}m$ (221)

These tilts and rotations are extremely sensitive to external conditions, including temperature, pressure and strain. This latter aspect is particularly important in the case of thin films which are epitaxially grown onto a suitable substrate. Considerable tensile or compressive strain in the film often arises because of mismatch between the lattice parameter of the substrate and the lattice parameter of the film. Such effects can cause considerable (and sometimes surprising) changes in the physical properties of the film itself or of the interface region. In addition, chemical substitution at A- and B-sites in a perovskite may significantly alter the tilt and rotation of

Table 1.3 *Lattice parameter equations for some tilt systems*

Tilt system	Space group	Lattice parameters
$a^0a^0a^0$ (23)	$Pm\bar{3}m$ (321)	$a = 2d$
$a^0a^0c^-$ (22)	$I4/mcm$ (140)	$a = (\sqrt{8})d\cos\varphi$, $c = 4d$
$a^0a^0c^+$ (21)	$P4/mbm$ (127)	$a = (\sqrt{8})d\cos\varphi$, $c = 2d$
$a^0b^-b^-$ (20)	$Imma$ (74)	$a = (\sqrt{8})d$, $b = 4d\cos\theta$, $c = (\sqrt{8})d\cos\theta$
$a^0b^-c^+$ (17)	$Cmcm$ (63)	$a = 4d\cos\theta$, $b = 2d(\cos\theta + 1)$, $c = 2d(\cos\theta + 1)$
$a^0b^+b^+$ (16)	$I4/mmm$ (139)	$a = 2d(1 + \cos\theta)$, $c = 4d\cos\theta$
$a^-a^-a^-$ (14)	$R\bar{3}c$ (167)	$a = (\sqrt{8})d\cos\phi$, $c = (\sqrt{48})d$
$a^+a^+a^+$ (3)	$Im\bar{3}$(204)	$a = (8\cos\phi + 4)/3$

the linked octahedra. For example, the octahedral tilt in such series as the lanthanoid nicklates, $LnNiO_3$, varies directly in proportion to the size of the lanthanoid cation and can be tuned by suitable A-site doping.

1.7.2 Trigonal Symmetry: $LaAlO_3$ as an Example

Trigonal perovskites, typified by the (3, 3) phase $LaAlO_3$ at room temperature, are produced by a rotation of the BO_6 octahedra by approximately 6° about a trigonal axis normal to a triangular octahedron face compared to the cubic parent structure (Figure 1.13a and b). (The crystal class of these phases is trigonal, while the axes are termed rhombohedral. The axes are often more conveniently described in terms of a hexagonal unit cell.) In terms of the tilts in Table 1.2, these compounds belong to the tilt system (14), $a^-a^-a^-$, with the octahedra in each successive layer tilted in opposite directions (Figure 1.13c).

$LaAlO_3$: trigonal, hexagonal cell; $a_H = b_H = 0.5365$ nm, $c_H = 1.3111$ nm, $\alpha = \beta = 90°$, $\gamma = 120°$, $Z = 6$; space group, $R\bar{3}c$ (167); using a hexagonal cell:

$$\begin{aligned}\text{Atom positions: } &\text{La}: 6(a)\, 0,0,¼; 0,0,¾;\\ &\text{Al}: 6(b)\, 0,0,0; 0,0,½;\\ &\text{O}: 18(c)\, x,0,¼; 0,x,¼; -x,-x,¼; -x,0,¾; 0,-x,¾;\\ &\qquad x, x, ¾;\ x = 0.5254 \text{ at } 320\text{ K}.\end{aligned}$$

The rotation angle diminishes as the temperature increases and becomes zero, giving the cubic structure (Figure 1.13a), at approximately 813 K with a lattice parameter of $a = 0.38113$ nm at 850 K. The octahedra are found to be slightly flattened down the triad (hexagonal c, rhombohedral [111]) axis, but the Al—O bond lengths are all equal at 0.190 nm.

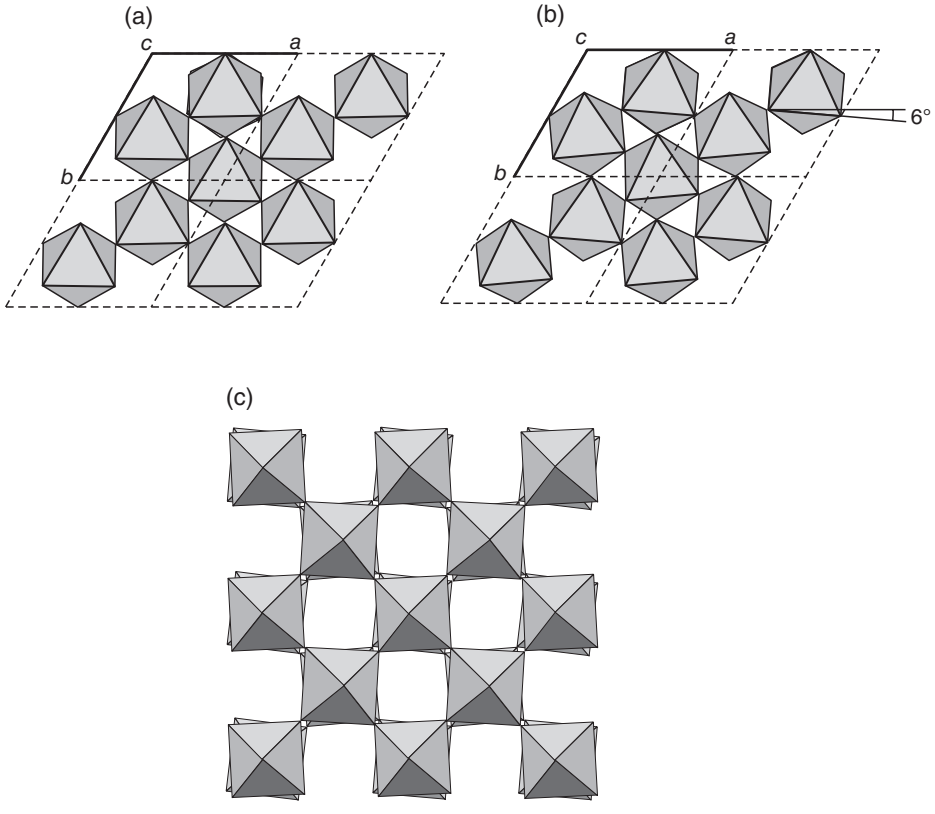

Figure 1.13 *The $LaAlO_3$ structure: (a) projection of ideal cubic structure down [001]; (b) projection of the $LaAlO_3$ structure down [001], with a rotation angle of 6°; (c) projection showing octahedral layer tilts*

It is possible to estimate the unit cell parameters using the formulae in Table 1.3. Taking d as half the $SrTiO_3$ unit cell edge, 0.195 nm:

$$a = \left(\sqrt{8}\right) d\cos\phi = \left(\sqrt{8}\right) \times 0.195 \times \cos 6 = 0.548 \text{ nm}$$

$$\text{c} = \left(\sqrt{48}\right) d = 1.316 \text{ nm}$$

which are in good agreement with the experimental values.

The structure can also be described in terms of a primitive rhombohedral cell:

$$a_{\text{RP}} = b_{\text{RP}} = c_{\text{RP}} = 0.5357 \text{ nm}, \alpha = \beta = \gamma = 60.1°, Z = 2$$

Table 1.4 *Phases with the trigonal $LaAlO_3$ structure*

Phase	Space group	*a* (nm)	*b* (nm)	*c* (nm)
$LaAlO_3$	*R*3*c* (161)	0.53644	0.53644	1.31195
$LaCoO_3$	$R\bar{3}c$ (167)	0.54437	0.54437	1.30957
$LaMnO_3$[a]	$R\bar{3}c$ (167)	0.55312	0.55312	1.3488
$La_{0.6}Sr_{0.4}MnO_3$	$R\bar{3}c$ (167)	0.55005	0.55005	1.33575
$LaNiO_3$	$R\bar{3}c$ (167)	0.54524	0.54524	1.31572
$LiNbO_3$	*R*3*c* (161)	0.51381	0.51381	1.38481
$LiTaO_3$	*R*3*c* (161)	0.51528	0.51528	1.37795

[a] Also reported as adopting the $GdFeO_3$ structure (Section 1.7.3).

The relationship between the dimensions of the two unit cells is

$$a_{RP} = \frac{1}{3}\sqrt{\left(3a_H^2 + c_H^2\right)}$$

$$\sin\left(\frac{\alpha}{2}\right) = \frac{3a_H}{2\sqrt{\left(3a_H^2 + c_H^2\right)}}$$

Finally the structure can also be described in terms of a face-centred rhombohedral cell:

$$a_{RF} = b_{RF} = c_{RF} = 0.7581\,\text{nm},\ \alpha = \beta = \gamma = 90.1°,\ Z = 8$$

The relationship between the dimensions of the hexagonal and face-centred rhombohedral unit cells is

$$a_{RF} = \frac{1}{3}\sqrt{\left(12a_H^2 + c_H^2\right)}$$

$$\cos\alpha = \frac{\left(c_H^2 - 6a_H^2\right)}{\left(c_H^2 + 12a_H^2\right)}$$

Despite the tilting, the unit cell is almost cubic; the pseudocubic cell having dimensions a_p = half the a_{RF} axis, 0.379 nm (Table 1.4).

Many of these perovskites revert to the ideal cubic structure at higher temperatures.

1.7.3 Orthorhombic Symmetry: $GdFeO_3$ and $CaTiO_3$ as Examples

The classical orthorhombic distorted perovskites are often referred to as being of the $GdFeO_3$ type, choosing the (3, 3) phase as the structure type. The octahedral

rotations in these phases are about the diad axes, [110], belonging to tilt system 10, $a^+b^-b^-$. $GdFeO_3$ has the crystallographic parameters:

$GdFeO_3$: orthorhombic; $a = 0.5349$ nm, $b = 0.5609$ nm, $c = 0.7669$ nm, $Z = 4$; space group, *Pbmn* (No. 62, nonstandard setting);

$$\begin{aligned}\text{Atom positions}: \quad & \text{Gd}: 4(a)\, 0.9846, 0.0629, ¼ \\ & \text{Fe}: 4(b)\, ½, 0, 0 \\ & \text{O1}: 4(c)\, 0.1116, 0.4569, ¼ \\ & \text{O2}: 8(d)\, x, y, z;\ x+½, -y+½, -z;\ -x, -y, z+½; \\ & \qquad -x+½, y+½, -z+½;\ -x, -y, -z;\ -x+½, y+½, z; \\ & \qquad x, y, -z+½;\ x+½, -y+½,\ z+½; \\ & \qquad x = 0.6960,\ y = 0.3021,\ z = 0.0521.\end{aligned}$$

Another example is provided by Perovskite itself, which is typical of the (2, 4) phases:

$CaTiO_3$: orthorhombic; $a = 0.5379$ nm, $b = 0.5436$ nm, $c = 0.7639$ nm, $Z = 4$; space group, *Pbmn* (No. 62, nonstandard setting);

$$\begin{aligned}\text{Atom positions}: \quad & \text{Ca}: 4(a)\, 0.9922, 0.0357, ¼ \\ & \text{Ti}: 4(b)\, ½, 0, 0 \\ & \text{O1}: 4(c)\, 0.0736, 0.4828, ¼ \\ & \text{O2}: 8(d)\, x, y, z;\ x+½, -y+½, -z;\ -x, -y, z+½;\ -x+½, y \\ & \qquad +½, -z+½;\ -x, -y, -z;\ -x+½, y+½, z;\ x, y, -z \\ & \qquad +½;\ x+½, -y+½, z+½; \\ & \qquad x = 0.7113,\ y = 0.2893,\ z = 0.0375.\end{aligned}$$

The nonstandard setting of the space group is often (but not universally) used for these structures (Table 1.5). In this setting, the orthorhombic unit cell is given the space group *Pbnm*, with $a < b < c$; $Z = 4$; A atoms are in the positions 4*c*; B atoms in 4*b*; O1 atoms in 4*c*; O2 atoms in 8*d*. In the standard setting, the orthorhombic unit cell is given the space group *Pnma*, with $a < b > c$; $Z = 4$; A atoms in positions 4*c*; B atoms in 4*b*; O1 atoms in 4*c*; O2 atoms in 8*d*.

At room temperature the structure of orthorhombic $CaTiO_3$ is due to the rotation of the TiO_6 octahedra about a diad axis, corresponding to the tilt group $a^+b^-b^-$ (Figure 1.14). As the temperature increases these distortions gradually diminish and eventually the orthorhombic phase transforms to tetragonal at 1498 K: space group *I*4/*mcm* (140), $a = b = 0.54984$ nm, $c = 0.77828$ nm. The octahedra are now much more regular, but still tilted, with a tilt system $a^0a^0c^-$. As the temperature continues to increase, these

Table 1.5 *Phases with the orthorhombic $GdFeO_3$ structure*

Phase	Space group	*a* (nm)	*b* (nm)	*c* (nm)
$NaFeF_3$	*Pnma* (62)	0.566119	0.788006	0.548359
$YAlO_3$	*Pbnm* (62)	0.518	0.531	0.735
$CaTiO_3$	*Pbnm* (62)	0.5379	0.5436	0.7639
$NdTiO_3$	*Pbnm* (62)	0.552532	0.565945	0.779066
$SmTiO_3$	*Pbnm* (62)	0.54647	0.56712	0.77291
$GdTiO_3$	*Pbnm* (62)	0.54031	0.57009	0.77133
$YTiO_3$	*Pbnm* (62)	0.53210	0.56727	0.75949
$TbCoO_3$	*Pbnm* (62)	0.51995	0.53945	0.74102
$DyCoO_3$	*Pbnm* (62)	0.51655	0.54143	0.77866
$CaRuO_3$	*Pnma* (62)	0.5544	0.7649	0.5354
$SrRuO_3$	*Pbnm* (62)	0.55754	0.55405	0.78546
$CaMnO_3$	*Pnma* (62)	0.52781	0.74542	0.52758
$Nd_{0.99}Ca_{0.1}CoO_3$	*Pnma* (62)	0.533379	0.755034	0.534640
$EuNiO_3$	*Pbnm* (62)	0.52945	0.54681	0.75404
$GdFeO_3$	*Pbnm* (62)	0.5349	0.5609	0.7669
$LaTiO_3$	*Pbnm* (62)	0.563676	0.561871	0.791615
$LaCrO_3$	*Pbnm* (62)	0.55163	0.54790	0.77616
$LaFeO_3$	*Pbnm* (62)	0.55563	0.55630	0.78535
$SrSnO_3$	*Pbnm* (62)	0.57042	0.57113	0.80674
$SrZrO_3$	*Pbnm* (62)	0.57093	0.57053	0.80676
$La(Fe_{0.5}V_{0.5})O_3$	*Pbnm* (62)	0.5552	0.5558	0.7836
$LaMnO_3$[a]	*Pbnm* (62)	0.55397	0.54891	0.77928
$CeMnO_3$	*Pbnm* (62)	0.5537	0.5557	0.7821
$PrMnO_3$	*Pnma* (62)	0.5608	0.7634	0.5442
$NdMnO_3$	*Pnma* (62)	0.57233	0.7587	0.54209
$SmMnO_3$	*Pbnm* (62)	0.53584	0.57959	0.74608
$EuMnO_3$	*Pbnm* (62)	0.53437	0.58361	0.746186
$GdMnO_3$	*Pbnm* (62)	0.53160	0.58683	0.74252
$DyMnO_3$	*Pbnm* (62)	0.531606	0.582304	0.738443
$HoMnO_3$	*Pbnm* (62)	0.52565	0.58329	0.73602
$ErMnO_3$	*Pbnm* (62)	0.52402	0.58228	0.73436
$TmMnO_3$	*Pbnm* (62)	0.52310	0.58157	0.73218
$YbMnO_3$	*Pbnm* (62)	0.52190	0.58038	0.73027
$LuMnO_3$	*Pbnm* (62)	0.518956	0.578498	0.72815
$La_{0.5}Ca_{0.5}MnO_3$	*Pnma* (62)	0.54182	0.76389	0.54269
$LaFe_{0.5}V_{0.5}O_3$	*Pbnm* (62)	0.55597	0.55571	0.78523
$NdFe_{0.5}V_{0.5}O_3$	*Pbnm* (62)	0.54497	0.55682	0.77516
$EuFe_{0.5}V_{0.5}O_3$	*Pbnm* (62)	0.53699	0.55975	0.76745
$YFe_{0.5}V_{0.5}O_3$	*Pbnm* (62)	0.52839	0.55969	0.75966

[a] Also reported as adopting the $LaAlO_3$ structure (Section 1.7.2).

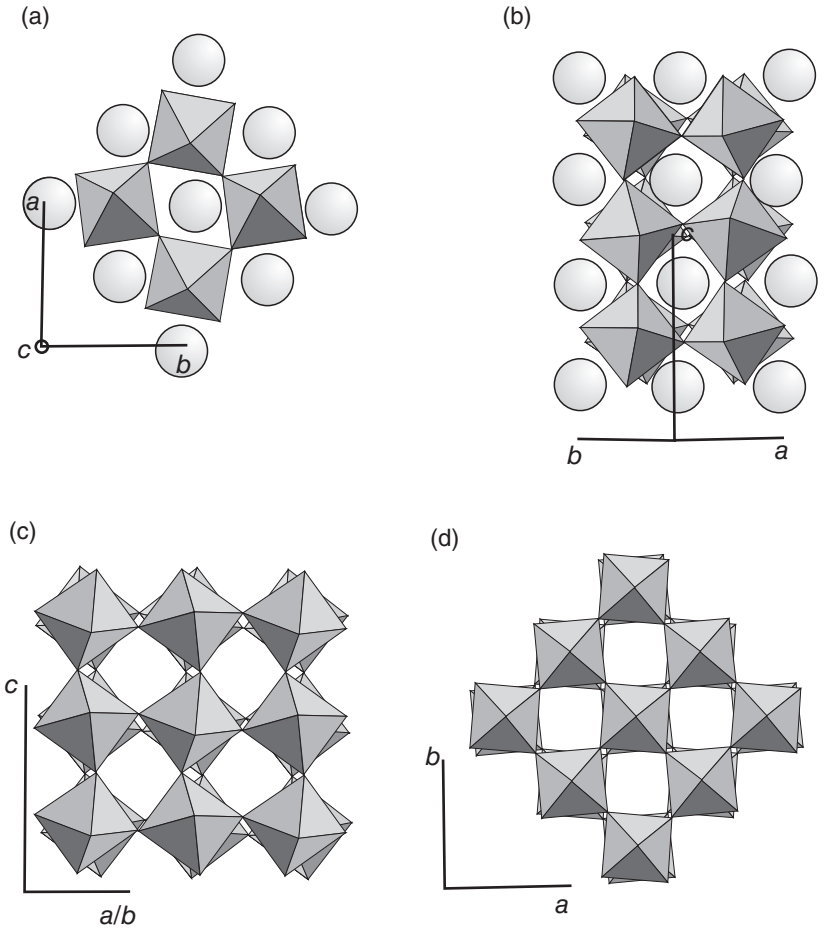

Figure 1.14 *The $GdFeO_3$-type structure of $CaTiO_3$: (a) projection down [001]; (b) projection down [110]; (c) projection down [110] showing octahedra only; (d) projection down [001] showing octahedra only*

remaining rotations diminish further, and the unit cell becomes cubic, space group $Pm\bar{3}m$ (221), $a = 0.38967$ nm, with a tilt system $a^0a^0a^0$, via a transition at 1634 K.

For many purposes it is adequate to describe $GdFeO_3$-type structures in terms of a pseudocubic cell, which in the *Pbnm* setting is $a \approx \sqrt{2}a_p$, $b \approx \sqrt{2}a_p$, $c \approx 2a_p$ with $a_p \approx 0.39$ nm. The B cations are nearly central in the octahedra, which are only slightly distorted (Figure 1.14a). The octahedral tilting, $a^+b^-b^-$, is noticeable in projections along [110] and [001] directions of the unit cell (Figure 1.14b–d). The octahedral tilting causes the ideal cuboctahedral sites to be reduced nearer to cubic antiprism geometry, with the A cation located in a space with 8 nearest neighbour oxygen ions and 4 anions at a greater distance rather than 12 equidistant anions.

1.8 Symmetry Relationships

When an ideal cubic perovskite, space group $Pm\bar{3}m$, drops in symmetry due to cation displacement, octahedral tilting and so on, some of the symmetry elements of the space group are lost. The space groups listed previously tend to obscure this aspect of the transformation. Group theoretical organisation of these into groups and subgroups makes the relationships clear and the possible subgroups that can apply when any particular distortion occurs can be enumerated by group theoretical methods.

This approach is of considerable value when new structures have to be determined. The diffraction patterns from slightly distorted perovskites show splitting of the main cubic reflections together with the appearance of new superstructure lines. However, when these distortions are very small, diffraction pattern changes are minute and the new superstructure reflections are weak. A listing of the possible subgroups simplifies the crystallographic problem by limiting the number of space groups that are compatible with any assumed distortions.

This procedure can be illustrated with respect to B-site cation displacements, described previously, assuming that the cation shift is the same in each octahedron. Using a notation that parallels the rotation notation given in Section 1.7.1 allows a displacement along x, y and z to be written as (a, b, c). If the displacement is the same along two axes, the letter symbol is repeated. Thus a displacement (0, 0, a) is along [001] and will preserve the fourfold rotation axis. A displacement (a, a, 0), obtained by translation of the cation by an amount a along both [100] and [010], will give a resultant along [110] and will preserve the diad axis. A displacement (a, a, a), obtained by translation of the cation by an amount a along [100], [010] and [001], will have a resultant along [111] and will preserve the triad axis (Section 1.5).

For example, displacement along [001] in original space group $Pm\bar{3}m$ will retain the fourfold rotation axis and so lead to a tetragonal space group, of which there are 68. Group theoretical analysis of the effects of the distortion limits this to just one, *P*4*mm* (99). Similar analysis shows that all permissible cation displacements lead to a hierarchy of just six subgroups (Figure 1.15).

A similar hierarchy can be constructed for the octahedral tilts described earlier. Group theoretical analysis of the symmetry of these tilt systems has led to the conclusion that 8 of the total of 23 tilts listed previously cannot be observed in real crystals and so are redundant in experimental terms. The remaining 15 are $a^0a^0a^0$ (23), $a^0a^0c^+$ (21), $a^0b^+b^+$ (16), $a^+a^+a^+$ (3), $a^+b^+c^+$ (1), $a^0a^0c^-$ (22), $a^0b^-b^-$ (20), $a^-a^-a^-$ (14), $a^0b^-c^-$ (19), $a^-b^-b^-$ (13), $a^-b^-c^-$ (12), $a^0b^+c^-$ (17), $a^+b^-b^-$ (10), $a^+b^-c^-$ (8), and $a^+a^+c^-$ (5). The hierarchy of these subgroups shows a decent in symmetry from the cubic parent $Pm\bar{3}m$ space group via tetragonal and orthorhombic to triclinic (Figure 1.16).

The 15 allowed transformations are imagined to operate alone. In reality many perovskite phases show additional octahedral cation displacements or distortions which will change things. For example, the tilt system 14, $a^-a^-a^-$ has an ideal trigonal space

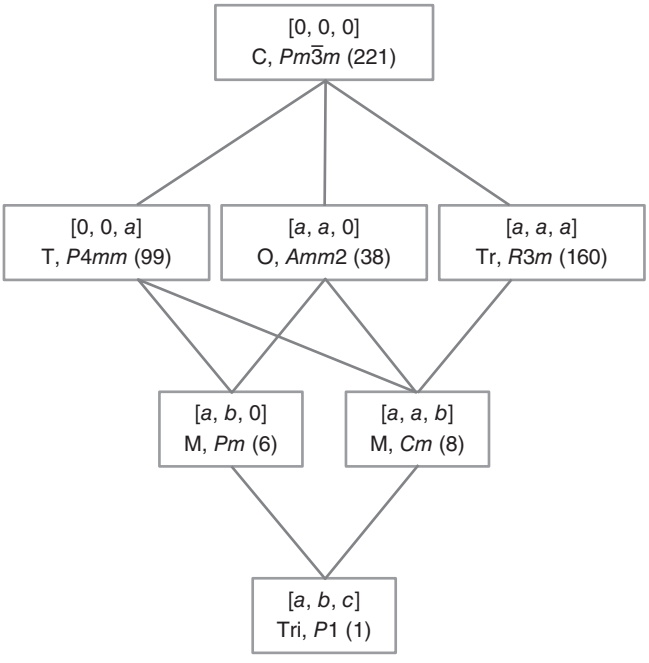

Figure 1.15 *Subgroups derived by displacement of the B-site cation from the parent space group* Pm3̄m. *The cation displacement along* x, y *or* z *is denoted by* a, b *or* c

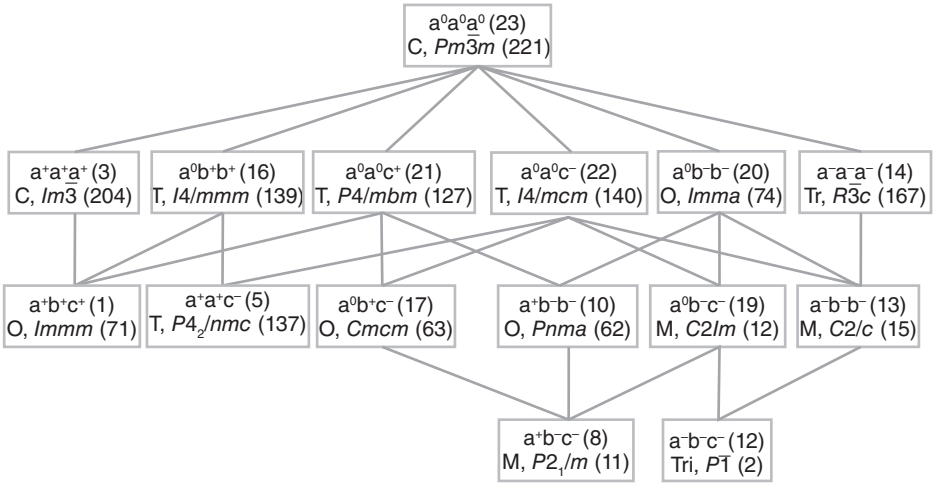

Figure 1.16 *The space groups allowed by the possible tilt systems of octahedra in pseudocubic perovskites*

group $R\bar{3}c$ (167) with a centre of symmetry. If the B cations that centre the octahedra are displaced, then the centre of symmetry is lost and the space group remains trigonal but is changed to *R*3*c* (161). Jahn–Teller distortions have a similar effect. $KCuF_3$ has no octahedral tilting and belongs to the tilt system 23, $a^0a^0a^0$ but does not possess the cubic space group $Pm\bar{3}m$ (221) of $SrTiO_3$ because of the elongation of the CuO_6 octahedra, as described earlier, to give a tetragonal cell, space group *I*4/*mcm* (140).

Table 1.6 *Organic–inorganic hybrid and related perovskites*

Phase	Space group	*a* (nm)	*b* (nm)	*c* (nm)	Angles (°)	Temp (K)
$CsSnI_3$	O, *Pnma* (62)	0.86885	1.23775	0.86384		300
$CsSnI_3$	T, *P*4/*mbm* (127)	0.87182		0.61908		350
$CsSnI_3$	C, $Pm\bar{3}m$ (221)	0.62057				478
$MAGeCl_3$	M, $P2_1/n$ (14)	1.09973	0.72043	0.82911	α, 90.47	2
$MAGeCl_3$	O, *Pmna* (62)	1.11567	0.73601	0.82936		250
$MAGeCl_3$	Tr, *R*3*m* (160)	0.56784			α, 90.95	370
$MAGeCl_3$	C, $Pm\bar{3}m$ (221)	0.56917				475
$CD_3ND_3GeCl_3$	M, $P2_1/n$ (14)	1.09973	0.72043	0.82911	β, 90.47	2
$CD_3ND_3GeCl_3$	O, *Pnma* (62)	1.11567	0.73601	0.82936		250
$CD_3ND_3GeCl_3$	Tr, *R*3*m* (160)	0.56584			α, 90.95	370
$CD_3ND_3GeCl_3$	C, $Pm\bar{3}m$ (221)	0.56917				475
$MASnCl_3$	Tri, *P*1 (1)	0.5726	0.8227	0.7910	α, 90.40 β, 93.08 γ, 90.15	297
$MASnCl_3$	M, Pc (7)	0.5718	0.8326	0.7938	β, 93.03	318
$MASnCl_3$	Tr, *R*3*m* (160)	0.5734			α, 91.90	350
$MASnCl_3$	C, $Pm\bar{3}m$ (221)	0.5760				478
$MASnBr_3$	O, $Pmc2_1$ (26)	0.58941	0.83862	0.82406		215
$MASnI_3$	T, *P*4*mm* (99)	0.62302		0.6231		293
$MASnI_3$	T, *I*4*cm* (108)	0.87577		1.2429		200
$MAPbI_3$	T, *P*4*mm* (99)	0.63115		0.63161		400
$MAPbI_3$	T, *I*4*cm* (108)	0.8849		1.2642		293
$MAPbI_3$	O, *Pmna* (62)	0.88362	1.25804	0.85551		100
$FASnI_3$	O, *Amm*2 (38)	0.63286	0.89554	0.89463		340
$FASnI_3$	O, *Imm*2 (44)	1.25121	1.25171	1.25099		180
$CH_3ND_3PbCl_3$	O, *Pnma* (62)	1.11747	1.13552	1.12820		80
$CH_3ND_3PbCl_3$	C, $Pm\bar{3}m$ (221)	0.5669				280
$CH_3ND_3PbBr_3$	O, *Pnma* (62)	0.79434	1.18499	0.85918		11
$MAPbI_3$	O, *Pnma* (62)	0.88362	1.25804	0.85551		100
$MAPbI_3$	T, *I*4/*mcm* (140)	0.8851		1.2444		298
$MAPbI_3$	C, $Pm\bar{3}m$ (221)	0.6274				333
$FAPbI_3$	Tr, *P*3*m*1 (156)	0.89817		1.1006	γ, 120	293

1.9 Hybrid Organic–Inorganic Perovskites

The A-sites in the perovskite structure are large enough to accommodate a number of complex ions including ammonium $(NH_4)^+$; methyl ammonium $(CH_3NH_3)^+$ frequently written as MA; tetramethylammonium, $[(CH_3)_4N]^+$, frequently written as TMA and formamidinium $(NH_2{=}CHNH_2)^+$, written as FA. The most important of these are the compounds formed with the Group 14 elements Ge, Sn and Pb, together with a halogen Cl, Br and I (Table 1.6). The valence state of the organic ion is +1, and this necessitates the B cation to adopt the +2 state. It is unusual to find these large B^{2+} ions in the octahedral B-sites, and they are more frequently associated with A-sites, as in lead titanate, $PbTiO_3$. A large electropositive cation is needed in the A-site to achieve this, which can include the inorganic cation Cs^+ as well as the ions above, and it is convenient to group the Cs halide perovskites with these inorganic–organic phases. The structure of these materials is typically slightly distorted cubic (Figure 1.17).

The organic groups can order or disorder and may have preferred orientations that could lead to orientational order–disorder transformations, with the concurrent formation of superlattices and smaller microdomains of order coherently

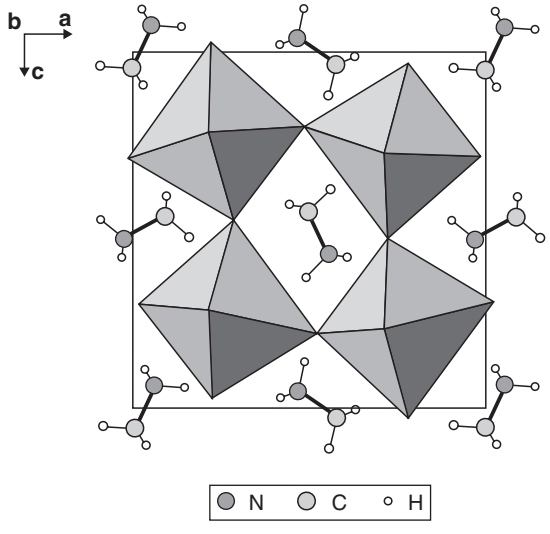

Figure 1.17 *The structure of $(CH_3NH_3)PbCl_3$ ($MAPbCl_3$). One layer of the structure is shown. In preceding and succeeding layers, the organic molecules are rotated by 180° compared to that drawn*

intergrowth within the crystal matrix (also see Section 2.6). This A-site ordering is sensitive to temperature. In addition, octahedral tilting and distortion, as described earlier, may also be present. As is usual, many of these structures show variation with temperature. The high-temperature polymorph is cubic, and as the temperature falls the symmetry drops as ordering and octahedral tilting becomes pronounced.

1.10 Antiperovskites

1.10.1 Cubic and Related Structures

The antiperovskite or inverse perovskite structure is adopted by many compounds with an overall composition A_3BX, where A and B are metals and X is typically C, N, O and B. There are two broad categories. The first, not described here, are essentially alloys containing interstitial nonmetal atoms in octahedral interstices; typical examples being Mn_4N, derived from the face-centred cubic structure of Mn, and Fe_3PtN, derived from the alloy Fe_3Pt, with the Cu_3Au structure.

The materials described here have structures quite different from a notional parent metallic phase and are more akin to the oxide and oxynitride perovskites already described. They can be described by a formula AMX_3, where A is from a wide range of metals including Al, Ga, In, Zn, Ge, Sn, Cu and others; M is either N or C and X is a metal, typically Mn, Cr, Fe, Ni, Ca, Ln and so on. The ionic model of use for the oxide perovskites is not, though, particularly appropriate for these phases; taking X to have a charge of 2+ (i.e. Ca^{2+}) or 3+ (i.e. La^{3+}, Mn^{3+}) and N to have a charge of 3– leads to improbable charge states for many A atoms (i.e. $CuNMn_3$), besides which, the large N^{3-} anion would not be expected to occupy the octahedral sites.

The structure of the majority of known phases is cubic, space group $Pm\bar{3}m$, with a lattice parameter of approximately 0.4 nm (Table 1.7). The structure is completely analogous to that of $SrTiO_3$, with the C or N nonmetal atom occupying an octahedron of A atoms, with X atoms at the cell corners (Figure 1.18).

$CuNMn_3$: cubic; $a = 0.3907$ nm, $Z = 1$; Space group, $Pm\bar{3}m$ (No. 221);

$$\begin{aligned}\text{Atom positions}: \ & \text{Cu}: 1(a)\ 0,0,0; \\ & \text{N}: 1(b)\ ½,½,½; \\ & \text{Mn}: 3(c)\ ½,½,0;\ ½,0,½;\ 0,½,½;\end{aligned}$$

The Mn atoms lie at the corners of the unit cell. The N atoms lie at the cell centre and are surrounded by a regular octahedron of Cu atoms.

Table 1.7 *Antiperovskite phases*

Phase	Space group	*a* (nm)	*b* (nm)	*c* (nm)
$CuNMn_3$	C, $Pm\bar{3}m$ (221)	0.3907		
$AlNTi_3$	C, $Pm\bar{3}m$ (221)	0.4110		
$GaNCr_3$	C, $Pm\bar{3}m$ (221)	0.3879		
$GaNMn_3$	C, $Pm\bar{3}m$ (221)	0.3903		
$BiNCa_3$	C, $Pm\bar{3}m$ (221)	0.48884		
$SbNCa_3$	C, $Pm\bar{3}m$ (221)	0.48541		
$PbNCa_3$	C, $Pm\bar{3}m$ (221)	0.49550		
$SnNCa_3$	C, $Pm\bar{3}m$ (221)	0.49460		
$GeNCa_3$	C, $Pm\bar{3}m$ (221)	0.47573		
$SnNLa_3$	C, $Pm\bar{3}m$ (221)	0.50948		
$SnNCe_3$	C, $Pm\bar{3}m$ (221)	0.50159		
$SnNPr_3$	C, $Pm\bar{3}m$ (221)	0.49753		
$SnNNd_3$	C, $Pm\bar{3}m$ (221)	0.49470		
$SnNSm_3$	C, $Pm\bar{3}m$ (221)	0.48835		
$InNCe_3$	C, $Pm\bar{3}m$ (221)	0.50416		
$PNCa_3$	O, *Pnma* (62)	0.67091	0.94518	0.66581
$AsNCa_3$	O, *Pbnm* (62)	0.67249	0.67196	0.95336
$AsNCr_3$	T, *I*4/*mcm* (140)	0.536		0.8066
$BiNSr_3$	C, $Pm\bar{3}m$ (221)	0.520691		
$MgCNi_3$	C, $Pm\bar{3}m$ (221)	0.38106		
$SbNSr_3$	C, $Pm\bar{3}m$ (221)	0.51725		
$BiNBa_3$	T, $P6_3/mmc$ (194)	0.76111		0.667919
$SbNBa_3$	T, $P6_3/mmc$ (194)	0.75336		0.66431
$NaNBa_3$	T, $P6_3/mmc$ (194)	0.84414		0.69817

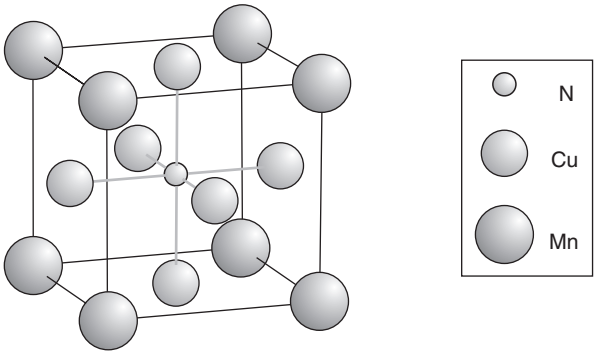

Figure 1.18 *The cubic antiperovskite structure of $CuNMn_3$*

The nitride antiperovskites show other structures, analogous to those displayed by oxide perovskites, but the number of known examples of these phases is minimal to date. The phases $PNCa_3$ and $AsNCa_3$ have tilted octahedra and belong to the $GdFeO_3$ structure type, tilt system $a^+b^-b^-$. $AsNCr_3$ is tetragonal with tilt system $a^0a^0c^-$.

Table 1.8 *Phases in the $BiNSr_{3-x}Ba_x$ and $SbNSr_{3-x}Ba_x$ systems*

Phase	Temperature (°C)	Cubic	4H	9R	2H
$BiNSr_{3-x}Ba_x$	875	$0<x<0.9$	$1.55<x<2.10$	$2.50<x<2.55$	$2.75<x<3.0$
$SbNSr_{3-x}Ba_x$	710	$0<x<1.3$	$1.83<x<2.45$	$2.56<x<2.60$	$2.80<x<3.0$

1.10.2 Other Structures

Two phases, $BiNBa_3$ and $SbNBa_3$, have been found to adopt the 2H─$BaNiO_3$ structure (Section 3.1). This structure, the hexagonal equivalent of the ideal perovskite structure, can form a bewildering array of phases consisting of intergrowths between hexagonal and cubic stacking in the oxide perovskites (Chapter 3, especially Section 3.5.1). In these antiperovskite materials, only two of these structure types are known, both formed in the cubic–hexagonal systems $BiNSr_3$ (cubic)–$BiNBa_3$ (hexagonal) and $SbNSr_3$ (cubic)–$SbNBa_3$ (hexagonal). These are the 4H structure and the 9R structure (for the structures see Section 3.5.1). The phase ranges of these materials at 875°C are given in Table 1.8.

1.11 Structure-Field Maps

Graphical displays of the way in which structures evolve as various physical parameters change have long been used to systematise structural relationships. It is convenient to use this idea to separate perovskite phases from other ABX_3 structure types and, if possible, to separate the different ABX_3 perovskite variants from each other. For this purpose the simplest parameters are the A- and B-cation radii. The relationship between these radii and the structure type found can be conveniently displayed on structure-field maps (see Muller and Roy 1974). These are equivalent to a graphical representation of the tolerance factor and usually refer to the structure stable under normal conditions (Figure 1.19a and b). There are a number of points to remember. First of all, the radii appropriate to the *y*-axis, associated with the A cations, should refer to 12-fold coordination. As such radii are not widely available, the figures here use eightfold radii on this axis. Similarly, the radii appropriate to the *x*-axis, associated with the B cations, should refer to octahedral coordination. Thus, for the $A^{3+}B^{3+}O_3$ diagram (Figure 1.19a), a lanthanoid ion on the *y*-axis will have a different radius than one on the *x*-axis. Surprisingly there is no extensive cubic structure phase field. The major phase field is that of compounds isostructural (or nearly so) with the $GdFeO_3$ structure type, but for the smallest B cations coupled with the largest A cations, the non-cubic $LaAlO_3$ structure predominates. Note that

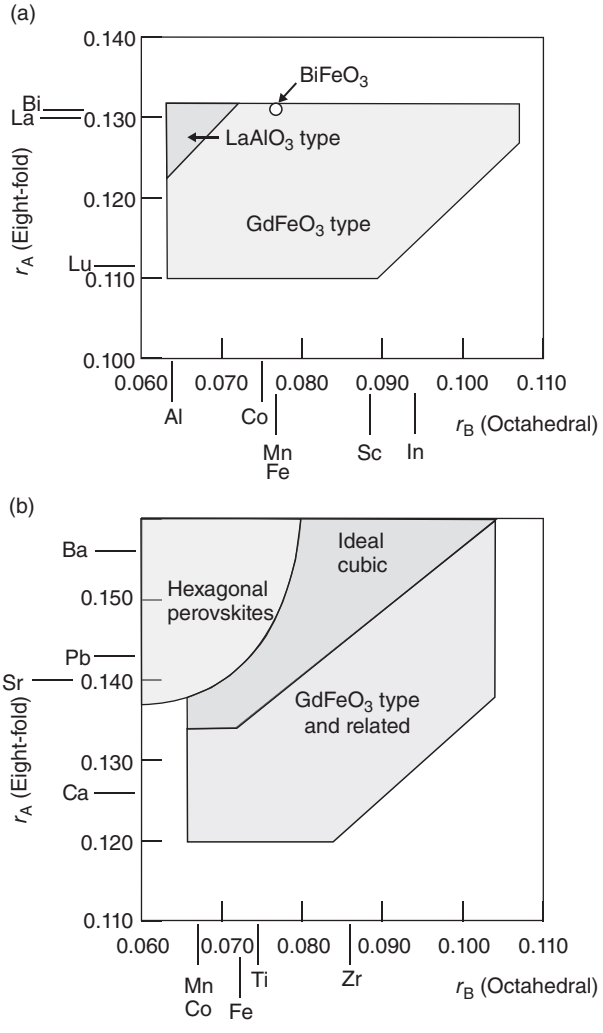

Figure 1.19 *Structure-field maps, schematic; r_A versus r_B: (a) $A^{3+}B^{3+}O_3$; (b) $A^{2+}B^{4+}O_3$ (Original data in Muller and Roy (1974))*

$BiFeO_3$ is somewhat anomalous. (Most Bi^{3+} compounds adopt the pyrochlore structure under normal conditions of temperature and pressure, not a perovskite-related structure. However, high pressures tend to convert these pyrochlores to distorted perovskite phases.)

The equivalent diagram for $A^{2+}B^{4+}O_3$ phases (Figure 1.19b) shows an extensive cubic phase field. There is a certain amount of overlap between the cubic phase field and the $GdFeO_3$-type phase field that is not shown in the figure drawn. A notable difference is the appearance of a hexagonal perovskite phase field for small B

cations coupled with large A cations (Chapter 3). Finally note that Pb^{2+} phases are similar to those of Bi^{3+} in that pyrochlore structure compounds form rather than perovskite types. The phases $PbZrO_3$ and $PbHfO_3$ are important exceptions to this generalisation.

These diagrams do not separate all phases precisely, and a number of efforts have been made to clarify the perovskite phase field more accurately. Recent efforts have used plots of the tolerance factor against the ratio of the radii of the B-site cation to the X-site anion as an octahedral factor:

$$\mu = \frac{r_B}{r_X}$$

for A_mO_n—B_mO_n oxide systems (Figure 1.20a) and AX—BX_2 halide systems (Figure 1.20b). These diagrams successfully demarcate most known AB combinations that lead to perovskite structure phase formation from those systems that do not.

Although structure-field maps do not predict the existence of the perovskite form with complete certainty, indicating that the factors that endow stability to this structure lie outside of simple radius correlations, the ease of the method makes it a simple and useful guide when unknown systems are being explored.

1.12 Theoretical Calculations

Information on formation energies or the electronic structure of single-phase perovskites can be assessed by quantum mechanical calculations. In the main, these take two forms, atomistic simulations and density functional theory calculations. Atomistic simulations are useful for the investigation of defect structures. Density functional methods are well-known tools for the estimation of stability and electronic structures. For example, experiment shows that $CaMnO_3$ has an orthorhombic $GdFeO_3$-type structure, in which all of the MnO_6 octahedra are apex linked; $BaMnO_3$ has the 2H-$BaNiO_3$ structure in which all of the MnO_6 octahedra are face sharing (Section 3.1). $SrMnO_3$ lies between these two extremes, with the 4H-structure, in which pairs of face-sharing octahedra are linked by apex sharing (Section 3.5). Density functional calculations reproduce these structures.

$CaMnO_3$: calculated, orthorhombic: $a = 0.53298\,\text{nm}$, $b = 0.74837\,\text{nm}$, $c = 0.52828\,\text{nm}$
experimental, orthorhombic: $a = 0.5281\,\text{nm}$, $b = 0.74542\,\text{nm}$, $c = 0.52758\,\text{nm}$

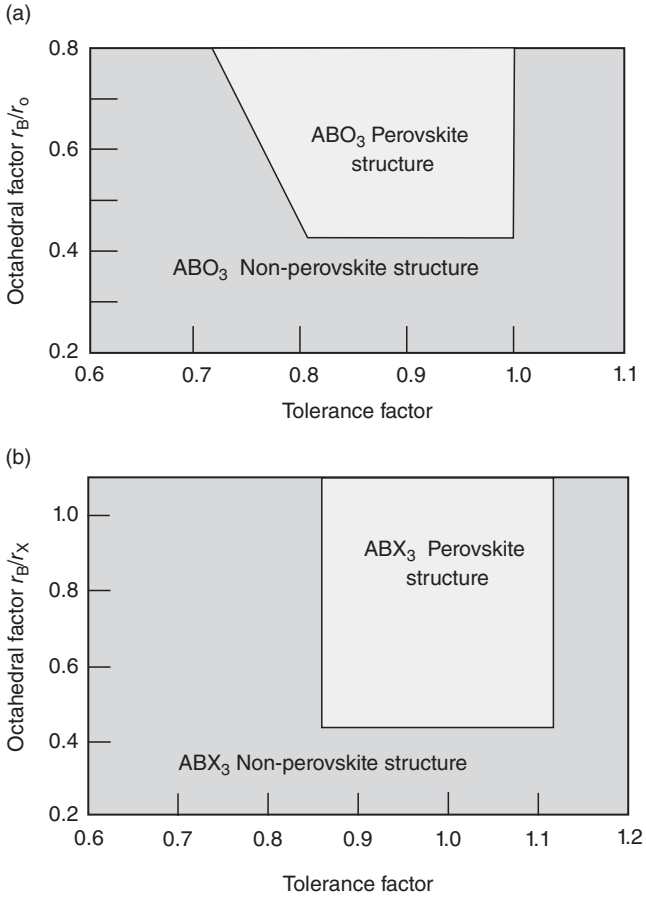

Figure 1.20 *Structure-field maps, schematic; tolerance factor* t *versus octahedral factor* μ*: (a) ABO_3 oxides; (b) ABX_3 halides (Original data in Li* et al. *(2008))*

The calculated stability order for $CaMnO_3$ is orthorhombic $GeFeO_3$, 4H-, cubic, 2H, in agreement with the experimental findings.

$SrMnO_3$: calculated, 4H: $a = 0.54893$ nm, $c = 0.91143$ nm
experimental, 4H: $a = 0.54432$ nm, $c = 0.90704$ nm

The calculated stability order is 4H, 2H, cubic so that the 4H structure is most stable, as found.

$BaMnO_3$: calculated, 2H: $a = 0.57781$ nm, $c = 0.48217$ nm
experimental, 2H: $a = 0.56691$ nm, $c = 0.48148$ nm

The calculated stability order is 2H, 4H, cubic in agreement with experimental data. (Data from Søndenå *et al.* (2007).)

Many other examples of density functional calculations mirror this example. These give good descriptions of the electronic properties of ground-state solids but still remain less successful at accurately predicting excited state properties.

References

A. M. Glazer, *Acta Crystallogr.*, **B28**, 3384–3392 (1972); Acta Crystallog., **A31**, 756–762 (1972).
S. A. Hayward, E. K. H. Salje, *J. Phys. Condens. Matter*, **14**, L599–L604 (2002).
T. Ishidate *et al*., *Phys. Rev. Lett.*, **78**, 2397 (1997).
C. Li *et al.*, *Acta Crystallogr.*, **B64**, 702–707 (2008).
O. Muller, R. Roy, *The Major Ternary Structural Families*, Springer-Verlag, Berlin (1974); p 175–196.
R. Søndenå *et al.*, *Phys. Rev.*, **B75**, 184105 (2007).

Further Reading

Earlier studies concerning the crystallography of perovskites are to be found in the following four volumes:

F. S. Galasso, *Structure, Properties and Preparation of Perovskite-Compounds*, Pergamon, London (1969).
B. G. Hyde, S. Andersson, *Inorganic Crystal Structures*, Wiley-Interscience, New York (1989); p 295–302.
H. Megaw, *Crystal Structures: A Working Approach*, Saunders, Philadelphia (1973); p 217–221, p 285–304.
O. Muller, R. Roy, *The Major Ternary Structural Families*, Springer-Verlag, Berlin (1974); p175–196.

More recent compilations are:

F. S. Galasso, *Perovskites and High T_c Superconductors*, Gordon & Breach, New York (1990).
R. H. Mitchell, *Perovskites: Modern and Ancient*, Almaz Press, Thunder Bay (2002).

For information on the early development of ferroelectric perovskite phases see:

L. E. Cross, R. E. Newnham, History of Ferroelectrics, in W. D. Kingery (Ed.), *Ceramics and Civilization, Vol III, High-Technology Ceramics–Past, Present and Future*, American Ceramic Society, Westerville (1987); p 289–305.

For information on the tolerance factor and structure-field maps see:

L. M. Feng *et al*., *J. Phys. Chem. Solids*, **69**, 967–974 (2008).
V. S. Goldschmidt, *Naturwissenschaften*, **21**, 447–485 (1926).
C. Li *et al.*, *Acta Crystallogr.*, **B64**, 702–707 (2008).
S. Sasaki, C. T. Prewitt, R. C. Liebermann, *Am. Mineral.*, **68**, 1189–1198 (1983).
Y. M. Zhang *et al*., *Mater. Focus*, **1**, 1–8 (2012).

Ionic radii are discussed and tabulated by:
R. D. Shannon, *Acta Crystallogr.*, **A32**, 751–756 (1976).
R. D. Shannon, C. T. Prewitt, *Acta Crystallogr.*, **B25**, 925–946 (1969); Acta Crystallogr., **B26**, 1046 (1970).

The systematics of octahedral tilt in perovskites is given by H. Megaw above and:
A. M. Glazer, *Acta Crystallogr.*, **B28**, 3384–3392 (1972); Acta Crystallog., **A31**, 756–762 (1972).
C. J. Howard, H. T. Stokes, *Acta Crystallogr.*, **B54**, 782–789 (1998).
M. O'Keeffe, B. G. Hyde, *Acta Crystallogr.*, **B33**, 3802–3813 (1977).
P. M. Woodward, *Acta Crystallogr.*, **B53**, 32–66, 44–66 (1997).

For information on the Jahn–Teller distortion in $KCuF_3$, see:
J.-S. Zhou *et al*., *J. Fluor. Chem.*, **132**, 1117–1121 (2011).

For a review of the $LnScO_3$ phases with the $GdFeO_3$ orthorhombic structure, see:
R. P. Liferovich, R. H. Mitchell, *J. Solid State Chem.*, **177**, 2188–2197 (2004)

For symmetry and group theory, see:
C. J. Howard, H. T. Stokes, *Acta Crystallogr.*, **B54**, 782–787 (1998).
C. J. Howard, H. T. Stokes, *Acta Crystallogr.*, **A61**, 93–111 (2005).
C. J. Howard, B. J. Kennedy, P. M. Woodward, *Acta Crystallogr.*, **B59**, 463–471 (2003).
M. C. Knapp, P. M. Woodward, *J. Solid State Chem.*, **179**, 1076–1085 (2006).
U. Müller, *Symmetry Relationships between Crystal Structures*, Oxford University Press, Oxford (2013).

For a review of antiperovskites, see:
R. Niewa, *Z. Anorg. Allg. Chem.*, **639**, 1699–1715 (2013).

For theoretical calculations see:
R. LeSar, *Introduction to Computational Materials Science*, Materials Research Society, Cambridge University Press, Cambridge (2013).
R. Søndenå *et al*., *Phys. Rev.*, **B75**, 184105 (2007).